LREE redistribution during hydrothermal alteration at the Okorusu carbonatite complex, Namibia

Delia Cangelosi [a,*], Sam Broom-Fendley [b], David Banks [a], Daniel Morgan [a], Bruce Yardley [a]

[a] School of Earth and Environment, University of Leeds, Leeds LS2 9JT, UK

[b] Camborne School of Mines, University of Exeter, Penryn Campus, Cornwall TR10 9FE, UK

Submission date: 7th May 2019

Abstract

The Cretaceous Okorusu carbonatite, Namibia, includes diopside-bearing and pegmatitic calcite carbonatites, both exhibiting hydrothermally altered mineral assemblages. In unaltered carbonatite, REE, Sr and Ba are largely hosted by calcite and fluorapatite. However, in hydrothermally altered carbonatites, small (< 50 µm) parisite-(Ce) grains are the dominant REE host, while Ba and Sr are hosted in baryte, celestine, strontianite and witherite. Hydrothermal calcite has a much lower trace element content than the original, magmatic calcite. Despite the low REE contents of the hydrothermal calcite, the REE patterns are similar to those of parisite-(Ce), and magmatic minerals and mafic rocks associated with the carbonatites. These similarities suggest that hydrothermal alteration

This is a 'preproof' accepted article for Mineralogical Magazine. This version may be subject to change during the production process.
DOI: 10.1180/mgm.2019.54

remobilised REE from magmatic minerals, predominantly calcite, without significant fractionation or addition from an external source. Ba and Sr released during alteration were mainly reprecipitated as sulfates. The breakdown of magmatic pyrite into Fe-hydroxide is inferred to be the main source of sulfate. The behaviour of sulfur suggests that the hydrothermal fluid was somewhat oxidising and it may have been part of a geothermal circulation system. Late hydrothermal massive fluorite replaced the calcite carbonatites at Okorusu and resulted in extensive chemical change, suggesting continued magmatic contributions to the fluid system.

KEYWORDS: REE, carbonatite, hydrothermal transport, Okorusu.

* ee12dac@leeds.ac.uk

1. Introduction

The rare earth elements (REE) are well known as 'critical metals' — metals which are sourced from a restricted region and have low substitutability and recyclability (Wall, 2014; European Commission, 2017; US Geological Survey, 2018). The largest and highest grade REE deposits are associated with carbonatite complexes (Chakhmouradian and Wall, 2012; Chakhmouradian and Zaitsev, 2012; Wall, 2014; Verplanck *et al.*, 2016). While this association demonstrates that magmatic processes are required for REE concentration, the REE as a group are also mobile in some hydrothermal fluids (Linnen *et al.*, 2014), and hydrothermal activity can play a major role in the development of economic concentrations of REE (e.g. Smith *et al.*, 2000, 2016).

A number of hydrothermally modified REE deposits have been recognised in a range of geological environments (e.g. Alderton *et al.*, 1980; Lewis *et al.*, 1998; Gysi and Williams-Jones, 2013). Indeed, the type-locality for several REE minerals, Bastnäs, is a skarn deposit

(Holtstam *et al.*, 2007; Holtstam *et al.*, 2014). Many carbonatites show evidence of hydrothermal reworking, which may be extensive (e.g. Wall *et al.*, 2008; Moore *et al.*, 2015; Broom-Fendley *et al.*, 2017a).

Evidence for hydrothermal mobility of REE comes from both experimental and natural studies of REE deposits (Perry and Gysi, 2018). Experimental studies indicate the solubility of REE is mainly determined by temperature and ligand availability (Williams-Jones *et al*., 2012). The stability of REE aqueous complexes with most ligands decreases along the lanthanide series, with light (L)REE (La to Sm) complexes more stable than the (H)REE (Migdisov *et al.*, 2016). Complexation by sulfate is the exception, with all REE-sulfate complexes having a similar stability (Migdisov and Williams-Jones, 2008). In most geological settings, the REE are believed to be predominantly transported as Cl^- complexes, reflecting the dominance of Cl^- over other potential ligands in most natural fluids (Banks *et al.*, 1994), as well as the greater solubility of REE-chloride complexes relative to fluoride, phosphate and carbonate complexes (Williams-Jones *et al.*, 2012).

Not all carbonatites show evidence of secondary fluid reworking. The REE can be hosted in apatite, a common carbonatite magmatic mineral for which the REE have a strong affinity (e.g. Giebel *et al.,* 2017). Apatite in carbonatites commonly contains over 1 wt. % total REE (Bühn *et al.*, 2003; Broom-Fendley *et al.*, 2016; Chakhmouradian *et al.,* 2017). REE may also be hosted in burbankite [$(Na,Ca)_3(Sr,Ca,REE,Ba)_3(CO_3)_5$] which commonly forms in a magmatic environment or close to the magmatic-hydrothermal transition (Zaitsev *et al.*, 1998, 2002; Moore *et al.,* 2015; Broom-Fendley *et al.,* 2017b). Wall (2014) however, noted that in carbonatite-related deposits, economic levels of REE are mainly contained in secondary minerals such as REE fluorcarbonates and monazite. The two main mechanisms

which may determine the economic viability of a carbonatite deposit for the REE are thus primary enrichment at the magmatic stage, which is predominantly controlled by apatite crystallisation, and secondary hydrothermal reworking.

In this study we investigate the mineralogy of the Okorusu Carbonatite Complex, Namibia, in order to understand the mechanism and scale of hydrothermal reworking of REE in a carbonatite. Although Okorusu is not a REE-rich carbonatite, the relatively small-scale alteration where REE contents are locally upgraded, provides an opportunity to understand the key processes. We report on how the REE are mobilised and concentrated from the magmatic to the late hydrothermal stages and investigate whether the locally elevated bulk REE contents are due to secondary enrichment from an external source or redistribution from nearby parts of the complex.

2. The Okorusu Carbonatite Complex

The Okorusu carbonatite complex is part of the Cretaceous Damaraland Igneous Province (~137 to 124 Ma), which is thought to be related to the Tristan da Cunha hot spot and the opening of the South Atlantic (Milner *et al.,* 1995). Okorusu has been dated to 126.6 ± 7.3 Ma (Milner *et al.,* 1995). The province comprises several intrusions of alkaline rocks and carbonatites trending northeast from the Cape Cross complex at the Atlantic coast (Fig. 1). Okorusu is the most north-easterly of this chain of intrusions and is located about 45 km NNE of the town of Otjiwarongo.

The detailed geological mapping by Van Zijl (1962) shows that it comprises a ring complex approximately 5 km by 6 km, consisting of syenite, nepheline syenite and carbonatite with an associated fenite aureole and hydrothermal fluorite mineralisation (Fig. 2). The country rocks adjacent to the complex are intruded by mafic dykes (Table 1), which are themselves

intruded by calcite carbonatite. The mafic dykes may be an early phase of the intruding igneous suite (Fig. 2). The main carbonatite bodies are medium-grained (0.25 mm to 2 mm) calcite carbonatites with white/grey calcite and accessory apatite and feldspar (Van Zijl, 1962; Bühn *et al.,* 2002). Shivdasan (2002) described two additional types of carbonatite: clinopyroxene carbonatite (diopside-bearing calcite carbonatite in this study), which has a silica content ranging from 9 wt. % to 12 wt. % and on average contains ~15 % volume pyroxene, and subordinate pegmatite carbonatite (pegmatitic calcite carbonatite in this study), characterised by a very coarse grain size (from 2 cm to > 20 cm), occurring as local pods or segregations within the diopside-bearing carbonatite.

The country rocks around the complex are regionally-metamorphosed sediments of the Pan-African Damara system, comprising schist, marble, conglomerate, and quartzite. Greywacke close to the carbonatites is locally fenitised to an alkali clinopyroxene-rich rock referred to as alkaline pyroxenite by Van Zijl (1962). The fenites themselves were subsequently altered by later hydrothermal activity, evidenced by fractures containing hydrothermal minerals including fluorite, alkali feldspar, magnetite, pyrite, apatite, quartz and calcite (Van Zijl, 1962).

For two decades, Okorusu was mined to extract fluorite for the production of HF; currently the mine is in care and maintenance. Fluorite mineralisation occurs in the high-grade fenite aureole in contact with Damara marbles, in calc-silicate lithologies, and in schists (Bühn *et al.,* 2002). Fluorite ore typically forms massive replacement textures. Other hydrothermal events occurred prior to fluorite deposition: magnetite and pyrrhotite hosted in the diopside-bearing carbonatite are hydrothermally altered with marcasite or hematite replacing pyrite and later magnetite (Shivdasan, 2002). Hydrothermal alteration of the

calcite carbonatite led to the introduction of euhedral quartz veins and growth of secondary minerals including synchysite [$CaLREE(CO_3)_2F$], baryte and fluorite (Shivdasan, 2002).

This study is based on detailed examination of two diopside-bearing calcite carbonatite pods (e.g. Fig. 3A), a pegmatitic calcite carbonatite pod about 11 m wide and 4 m high (Fig. 3B), a mafic dyke (sample OKC4) and a fluorite body (Fig. 2). Cerium is the dominant lanthanide in all the REE minerals identified at Okorusu; hence, the suffix–(Ce) will be omitted from mineral names for simplicity.

3. Methodology

Samples were collected from the Okorusu Fluorite Mine in October 2015. The mine comprises several pits (outlined in Fig. 2), which display differences in fluorite grade, grain size, colour and mineral associations. For the purposes of this study, which focusses on hydrothermal alteration in the carbonatites, these differences in the nature of the fluorite ore are of secondary importance. Samples collected from Pits A and C are labelled as OKA and OKC respectively (Fig. 3).

Mineral paragenetic relationships were established using optical petrography of thin sections and corresponding doubly polished wafers together with scanning electron microscopy (SEM), back scattered electron (BSE) and SEM-Cathodoluminescence (SEM-CL) imaging carried out at the University of Leeds using a FEI Quanta 650 Field Emission Gun Scanning Electron Microscope operated at 20 kV.

Mineral compositions were determined with a JEOL JXA8230 Electron Microprobe (EPMA) at the University of Leeds. Beam conditions were: 15 µm spot, 15 kV, 3 nA (calcite); 10 µm, 15 kV, 8 nA (apatite and fluorite); and 1 µm, 20 kV, 30 nA (diopside). The standards and element lists used for the different minerals are summarised in Appendix 1 alongside the

detection limit and on-peak and off-peak counting times for each element. Slight fluctuations in detection limits reflect the individual background measurement for each analysis. The selection of standards was aimed to match the structure of the unknown as closely as possible, using available material. Data reduction was with the Phi-Rho-Z Armstrong matrix correction (Packwood and Brown, 1981).

Complementary trace element data for minerals were obtained by Laser Ablation Inductively Coupled Plasma Mass Spectrometry (LA-ICP-MS) using a 193 nm ArF Excimer laser coupled to an Agilent 7500c ICP-MS instrument at the University of Leeds. Analyses were performed using a spot size from 25 to 51 µm, a 10 $J \cdot cm^{-2}$ laser fluence and a repetition rate of 5 Hz. The analyses were run in reaction cell mode using 2.5 $ml \cdot min^{-1}$ H_2 to supress $^{40}Ar^+$ and $^{40}Ar^{16}O^+$ interferences on $^{40}Ca^+$ and $^{56}Fe^+$ and improve the measurement of ^{39}K by removing the small interferences from ^{39}Ar. The following isotopes were analysed: ^{23}Na, ^{24}Mg, ^{29}Si, ^{39}K, ^{40}Ca, ^{47}Ti, ^{55}Mn, ^{56}Fe, ^{88}Sr, ^{89}Y, ^{238}Th, ^{232}U ^{137}Ba, ^{139}La, ^{140}Ce, ^{141}Pr, ^{146}Nd, ^{147}Sm, ^{153}Eu, ^{157}Gd, ^{159}Tb, ^{163}Dy, ^{165}Ho, ^{166}Er, ^{169}Tm, ^{172}Yb, ^{175}Lu. The element lists used per run alongside the limit of detection for each element are summarised in Appendix 1. The instrument was calibrated using NIST610 and NIST612 silicate glass standards, and these were ablated 6 times each at the beginning and end of each analysis session to monitor instrument drift, which was found to be insignificant. Because the LA-ICP-MS yields wt/wt ratios, the value of Ca (for carbonates, apatite and fluorite) or Si (for silicate minerals) was determined by EPMA in order to quantify the other elements analysed by LA-ICP-MS. Where this was not possible at a particular spot, the median concentrations of Ca or Si determined in nearby areas were used. For parisite [$Ca(LREE)_2(CO_3)_3F_2$], the stoichiometric Ca content was used to normalise analyses, since it was not analysed by EPMA. The ablation locations in each sample were the same as the locations of previous EPMA analyses.

Bulk rock analyses were undertaken by Activation Laboratories Ltd. with the sample preparation undertaken at the University of Leeds. Samples were powdered using a steel pestle and mortar and an agate TEMA barrel, and sieved to < 200 µm. The methods 4Litho and 4F-ISE were used on the calcite carbonatite and mafic dyke samples and the method 4Litho was used for the fluorite ore samples. The methods and detection limits are detailed in Appendix 2.

4. Field relationships and mineral paragenesis

Diopside-bearing and pegmatitic calcite carbonatites are the two main carbonatite types sampled for this study (Table 1). They record evidence of both magmatic crystallisation of the carbonatite magma and subsequent hydrothermal activity which led to the development of the present REE minerals. The mineralogy of the samples investigated is detailed in Table 1 and outlined below.

Diopside-bearing calcite carbonatites locally intrude marble country rock, and where this occurs they exhibit a magnetite aureole (Fig. 3A). Sample OKA5 is referred to as "least altered diopside-bearing calcite carbonatite" owing to its high percentage of magmatic minerals. "Altered, diopside-bearing calcite carbonatite" (sample OKA1, Fig. 3A) is a diopside-bearing calcite carbonatite which has undergone partial replacement of magmatic minerals by hydrothermal phases.

Pegmatitic calcite carbonatites occur as small pods within diopside-bearing calcite carbonatite, cementing brecciated diopside-bearing calcite carbonatite and in contact with fenite (Hagni and Shivdasan, 2001; Shivdasan, 2002), making it the last carbonatite type to form. Four samples and sub-samples are from a pegmatitic calcite carbonatite pod (Fig. 3B). The highly altered margins of this pod comprise ~95 % of hydrothermal minerals (sample

OKC19-2) and is referred to as “intensely altered calcite carbonatite” in the rest of this study (Fig. 3B). The degree of alteration is less intense in the interior of the pod.

Four phases of mineral growth have been identified: magmatic (stage 1), late magmatic (stage 2), hydrothermal (stage 3) and late hydrothermal fluorite mineralisation (stage 4). The textural relationships that determine the sequence of mineral growth are illustrated in Figs 4 and 5, while the mineral paragenesis is summarised in Fig. 6.

4.1 Stage 1 and 2—Magmatic to late magmatic minerals in the calcite carbonatites

The Okorusu calcite carbonatites predominantly exhibit magmatic textures typical of carbonatites (Chakhmouradian *et al.,* 2016). Magmatic calcite occurs as very large (0.5 cm to > 7 cm) twinned crystals and makes up the bulk of all carbonatite types. Magmatic calcite is distinguished from stage 3 hydrothermal calcite because it appears brighter in BSE images due to its higher level of Sr (Fig. 4B,D), and does not contain inclusions of baryte, strontianite or other sulfates or carbonates.

Clinopyroxenes in the diopside-bearing calcite carbonatite are diopside and occur as clusters of subhedral to euhedral crystals. Euhedral grains often display growth zoning while zoning in subhedral grains is less regular (Fig. 4A,B). Diopside commonly exhibits resorption along its edges, and occurs in two forms: evenly distributed through the least altered diopside-bearing calcite carbonatite (Fig. 4A,B) or segregated as diopside-rich clusters in the altered diopside-bearing calcite carbonatite. Diopside inclusions with resorbed edges occur in magmatic apatite and calcite suggesting that diopside was early to crystallise from the carbonatite magma (Fig. 6).

Apatite is the most significant magmatic REE-bearing mineral in the Okorusu calcite carbonatites. Stage 1 and 2 apatite occurs as medium-grained subhedral crystals (Fig. 4A,E),

locally radiating in clusters within apatite-rich zones typical of the diopside-bearing calcite carbonatite, but also as individual grains in contact with calcite (Fig. 4D), as inclusions in Ti-bearing magnetite (Fig. 4E) and Nb-bearing phases, or as vein-like clusters in the pegmatitic calcite carbonatite. The grains consistently exhibit similar textures, including complex zoning (Fig. 4B,M,O), with SEM-CL imaging revealing a pill-like shape typical of plutonic carbonatite (Chakhmouradian *et al.,* 2017, their fig. 5b), calcite inclusions (Fig. 4B,C). Magmatic apatites host inclusions of magmatic calcite and vice versa, indicating these minerals are cogenetic (Fig. 6).

Apatite records a complex growth history revealed by SEM-CL imaging. Some oscillatory growth zoning is present (Fig. 4M-O) and the apatite SEM-CL patterns indicate that dissolution was interspersed with periods of growth (Fig. 4M,O). Dissolution made stage 1 apatite (dull CL), porous, and the pores were then infilled with stage 2 apatite (bright CL) which truncates stage 1 zoning (Fig. 4M,O).

Similar textures in fluorapatite have been generated in hydrothermal experiments and have been ascribed to simultaneous dissolution–reprecipitation which creates porosity allowing enhanced transport and new growth (Harlov and Förster, 2003; Harlov *et al.,* 2005). Harlov *et al.,* (2005) describe topotaxial replacement of REE-bearing fluorapatite by a REE-depleted fluorapatite triggered by dissolution-reprecipitation in a HCl-H_2SO_4 solution. Chakhmouradian *et al.,* (2017) also describe very similar dissolution–reprecipitation texture in magmatic apatite, interpreted as apatite re-equilibration with a fluid. The Okorusu stage 1 and 2 apatites similarly have uniform extinction. Stage 2 growth is a 3D process, which creates the irregular patches observed in SEM-CL imaging (Fig. 4M,O). SEM-CL patterns

show that stage 1–stage 2 apatite relationships are consistent across the sample suites, irrespective of later alteration.

A few parisite crystals have developed on the edges of some magmatic apatites where it appears that part of the apatite was dissolved to crystallise parisite (Harlov and Förster, 2003; Harlov *et al.,* 2005) (Fig. 4N). Stage 2 apatite therefore has a cogenetic parisite generation.

Stage 2 apatite dissolution–reprecipitation may be driven by fluid exsolved from the crystallising carbonatite (Feng *et al.,* 2016) or might be post magmatic. While evidently formed after almost all the magmatic minerals, stage 2 apatite can occur entirely enclosed in magmatic calcite, with no post-magmatic hydrothermal calcite nearby, especially in the least altered calcite carbonatite (Fig. 4O,P). The lack of any later modification of adjacent magmatic calcite suggests that stage 2 apatite formed at the final magmatic stage while magmatic calcite was still stable. Both stage 1 and 2 apatites are replaced during later stage 3 hydrothermal alteration (Fig. 4E,L). In view of these observations, we believe that stage 2 apatite growth (and the associated parisite, Fig. 4N) did not form during the later stage 3 hydrothermal event.

Additional magmatic phases in the calcite carbonatites include phlogopite (which may host apatite and diopside inclusions), pyrite, which occurs as medium sized (~400 μm) subhedral crystals with apatite inclusions in sample OKA5 (< 5 %, Fig. 4G) and Ti-bearing magnetite. A few crystals of a heavily-altered euhedral Nb-bearing mineral with oscillatory zoning were also observed in the pegmatitic calcite carbonatite. The centres of the Nb-bearing crystals are heavily altered and porous, but Nb is present throughout the grain. The least altered parts give an EDS spectrum dominated by Nb with associated peaks for Sr, Ti, Ca, Th and Fe.

The association of calcite, apatite and iron oxide is typical of carbonatites (Le Bas and Srivastava, 1989; Kapustin, 1980; Chakhmouradian *et al.,* 2016). Based on textures such as those illustrated in Fig. 4, we infer that the sequence of crystallisation was diopside joined by calcite, apatite and finally phlogopite (Fig. 6) (c.f. Weidendorfer et al 2017).

Silicate domains of intergrown plagioclase (ranging from albite to oligoclase in composition) and phengite with minor phlogopite, dolomite and calcite occur in the least altered diopside-bearing calcite carbonatite (Fig. 4C). At the edges of the silicate domains, coarser-grained diopside and calcite tend to be intergrown with the plagioclase (Fig. 4C). It is likely that these silicate domains are wall rock xenoliths which have reacted with the carbonatite magma (c.f. Anenburg *et al.,* 2018a; Chebotarev *et al.,* 2019).

4.2 Stage 3— Hydrothermal alteration

All carbonatite samples show some degree of secondary overprinting from hydrothermal fluids. In less-altered examples (e.g. OKA5, Fig. 4B,C), significant magmatic calcite remains, while in the most altered, OKC19-2, the magmatic calcite is fully replaced by coarse hydrothermal calcite with distinctive Ba, Sr and REE-bearing mineral inclusions (Fig. 4D). In detail, hydrothermal calcite is designated as stage 3a since it is, in turn, partially replaced by a spongy matrix of hydrothermal phases assigned to stage 3b (Fig. 4H). Apatite is also brecciated in altered areas and stage 3 calcite and quartz have crystallised in the gaps. In the most altered carbonatites, only minor magmatic apatite remains (Fig. 4L). Parisite is an integral part of stage 3 alteration, occurring in stage 3b spongy intergrowths as well as in stage 3a.

Hydrothermal (stage 3) calcite appears dark in BSE images compared to magmatic calcite as a result of low Sr and Ba contents (Table 2). In the least altered samples, stage 3 calcite is

confined to secondary replacement of magmatic calcite along cleavage planes and grain margins (Fig. 4B,D). Where alteration is more extensive, stage 3a calcite pseudomorphs stage 1 calcite (Fig. 4D). In all cases, stage 3a calcite contains small inclusions (from < 40 µm to < 10 µm for the least altered samples) of strontianite, witherite, parisite, baryte, celestine and unidentified REE-fluorcarbonate and REE-carbonate (Figs 4B,D, 6). In the pegmatitic calcite carbonatite, stage 3a calcite is more abundant and the inclusions are coarser (50 µm to 300 µm) towards the contact with the intensely altered calcite carbonatite (OKC19-2) where the magmatic calcite was fully replaced by stage 3a calcite.

The stage 3a inclusion phases, such as celestine, baryte and parisite (Fig. 6), can also occur with iron hydroxides (Fig. 4E) and quartz in the rock matrix. The hydrothermal iron hydroxide may be goethite or limonite. Iron hydroxides occur infilling fractures and replacing magmatic apatite (Fig. 4E). In the altered diopside-bearing calcite carbonatite, medium-grained apatite is locally brecciated and infilled with stage 3 quartz and parisite (Figs 4F, 6). Apatite is the only magmatic mineral remaining in the intensely altered calcite carbonatite (OKC19-2; Fig. 3B); it is brecciated and in-filled by stage 3a calcite with minor baryte, strontianite, celestine and iron hydroxide (Fig. 4L). Apatites are locally dissolved where stage 3a parisite has crystallised (Fig. 4F). Despite stage 3 alteration, some apatite crystals which were extensively altered still have unaltered regions which retain the CL pattern of stage 1 (oscillatory grey SEM-CL) and stage 2 apatite (bright SEM-CL) seen in less altered samples.

Stage 1 pyrite and Ti-bearing magnetite are partially replaced by stage 3 iron hydroxide minerals (Fig. 4E,G) while the Nb-bearing phases in the pegmatitic calcite carbonatites are heavily overprinted by stage 3 alteration, including growth of celestine in the rims. Minor

fluorite occurs in stage 3, where it appears to be cogenetic with iron hydroxide, replacing stage 1 pyrite and partially replacing stage 3a calcite in both calcite carbonatite types (Fig. 4J).

Stage 3b overprints stage 3a (Fig. 4H), and is characterised by the development of a spongy assemblage of porous dolomite and K-feldspar, with quartz, iron hydroxide, celestine, baryte, and accessory parisite, pyrite, Ti-oxide and sphalerite. The texture of the porous dolomite and K-feldspar contrasts with stage 3a calcite which is well crystallised, but it is likely that stage 3 dolomite coexisted with calcite (Fig. 4I). Stage 3 REE minerals, mainly parisite and other REE-carbonates, occur as inclusions in stage 3a calcite, in cracks cutting and replacing both stage 1 and 2 apatite (Fig 4E-F), and in altered diopside.

Stage 3 alteration products are coarser grained in the more intensely altered rocks, with parisite forming euhedral crystals up to 400 µm long in OKC19-2 (Fig. 4K). Intensely altered calcite carbonatite has the highest content of secondary sulfate minerals, with stage 3 anhedral strontianite commonly hosting baryte inclusions.

4.3 Stage 4— Fluorite mineralisation.

Massive fluorite replaces country rock marble as well as carbonatite bodies at Okorusu (Hagni and Shivdasan, 2000) and is described here as stage 4 alteration, although the scale of change in rock composition is much greater than for stage 3 alteration. Optical and SEM-CL imaging indicate three main fluorite generations formed during stage 4. The earliest fluorite, type 4a, occurs as small cubes (average 0.5 mm), typically exhibiting oscillatory growth zoning. Type 4b fluorite comprises coarse euhedral crystals (≥ 1 cm) in voids; which can be divided into an earlier, unzoned stage (type 4b-1) and later (type 4b-2) material with oscillatory euhedral growth zoning (Fig. 5A). Type 4a and 4b fluorite often developed

sequentially (Fig. 5A). Finally, type 4c fluorite seals healed cracks which crosscut the earlier fluorite generations.

Minor amounts of other minerals may accompany stage 4 fluorite, mainly growing between type 4a and type 4b fluorite, although these are not always present (Fig. 5). Type 4a fluorite is overgrown by a veneer of quartz, itself overgrown by dolomite, minor iron hydroxide and stage 4 calcite. The coexistence of quartz and dolomite requires a low temperature for this stage. This sequence of minerals was subsequently corroded and partially replaced by quartz, K-feldspar and minor baryte (Figs 5B, 6) prior to the growth of Type 4b fluorite. Bühn *et al.* (2003) divided the fluorite into types based on hand specimens and fluorite textures, whereas we have categorised them based on SEM-CL images. Type 4a fluorite from this study matches fluorite they observed in the metasomatised wallrock, while type 4b fluorite corresponds to their fluorite II. They also described feldspar and quartz with resorbed grains boundaries, but interpreted these textures as possible relicts of feldspar-bearing protoliths or as fluorite cogenetic phases observed in the metasomatised wall rock. Early fluid inclusion studies of the fluorite ore at Okorusu (Roedder, 1973), and subsequent work (Bühn *et al.,* 2002), yielded fluid salinities up to 5 wt. % NaCl equivalent and homogenisation temperatures between 120 °C to 150 °C.

While the stage 4 mineral assemblage is dominated by fluorite (Table 1) it contains a similar mineral suite to stage 3b, with coexisting calcite and dolomite, parisite, fluorite, baryte, quartz, iron hydroxide and K-feldspar in both stages. Stage 4 may fully replace the partially altered stage 3 calcite carbonatites (Hagni and Shivdasan, 2000). Overall, the fluorite orebody replaces calcite. If this process occurred without addition or removal of Ca, it implies a solid volume decrease of 33.5 % (Glover and Sippel, 1962), which would likely

result in an increase in porosity and so enhance fluid flow via a positive feedback. Some such feedback may explain the formation of the coarse euhedral stage 4b fluorite which crystallised in the voids created by the replacement process.

Rare earth mineralisation during stage 4 alteration occurs solely in association with type 4a fluorite. This contains discrete inclusions and elongate crystals of parisite embedded in cavity linings (Fig. 5C), crosscutting quartz and K-feldspar or associated with baryte as radiating crystals locally growing into the baryte (Fig. 5D).

5. Mineral compositions and trace element abundancies

5.1 Stage 1 magmatic phases

Calcite

Calcite is the most abundant magmatic phase in the Okorusu carbonatite. In both the diopside-bearing and pegmatitic calcite carbonatites the $CaCO_3$ component > 95 %. In detail, magmatic calcite in the least altered diopside-bearing calcite carbonatite has slightly lower Mg and Fe contents than magmatic calcite in other samples (Table 2). As with calcite carbonatites elsewhere (Chakhmouradian *et al.,* 2016; Chakhmouradian *et al.,* 2017), magmatic calcite has a high Sr content (usually > 2 wt % SrO; Table 2) with Ba as the next most abundant cation. The ∑LREE content tends to be higher in pegmatitic calcite carbonatite than diopside-bearing calcite carbonatites (respectively averaging ∑LREE= 1350 ppm and ∑LREE= 910 ppm, La and Ce are the most abundant lanthanides). Overall, ∑HREE (∑HREE= Eu–Lu) contents are low in magmatic calcite averaging < 20 ppm (Table 2), comparable to magmatic calcite from calcite carbonatites elsewhere (Chakhmouradian *et al.,* 2016) (Table 2). The calcite analyses are presented in Appendix 3.

Diopside

Diopsides are formally part of the diopside group and range into ferrian and ferro sodian diopside (Sturm, 2002). Most of the diopsides have Na_2O ranging from 0.75 wt. % to 1 wt. %, although some grain cores of ferro sodian diopside have Na_2O up to 2.25 wt. %. Diopside in the carbonatites is clearly distinct from aegerine which is typical of fenite (Zharikov *et al.,* 2007); this implies that the diopside is magmatic, as indicated by the textures. Diopside EPMA and LA-ICP-MS analyses are presented in Appendix 3. The diopside has low concentrations of REE (∑REE ranging from 11-135 ppm) with the heaviest REE lower than the limit of detection. Compared to the other minerals it shows a LREE enriched profile but the LREE pattern is flattened with Ce(cn) > La(cn), this curvature is characteristic of clinopyroxene from carbonatites (Reguir *et al.*, 2012) (Fig. 7).

Apatite

Semi-quantitative analyses confirm that apatites are fluorapatites which are the main magmatic host for the REE at Okorusu (Fig. 7). Apatites from the diopside-bearing and pegmatitic calcite carbonatites are similar in composition and comparable to apatites from other carbonatites (Chakhmouradian *et al.,* 2017; Belousova *et al.,* 2002), although Sr is relatively high (1.5 to 2 wt. % SrO; Table 3). In contrast, apatite inclusions hosted in magmatic calcite from the calcite carbonatite replacing the mafic dyke core (OKC4, Table 1), are distinctly enriched in Na and the REE but are depleted in Th (Table 3).

The narrow textural zonations made it difficult to analyse individual apatite growth stages (Fig. 4M,O), especially by LA-ICP-MS, but some individual analyses of stage 1 and 2 apatite are provided in Appendix 3. Stage 2 apatite has lower concentrations of the REE relative to stage 1, especially for the LREE (Fig. 8), and this may reflect the crystallisation of cogenetic parisite. Since both stages of apatite have very similar normalised REE trends (Fig. 7) despite

the differences in concentrations, exchange of REE with an external reservoir can likely be ruled out.

5.2 Stage 3: chemical changes accompanying hydrothermal alteration of calcite

Calcite

Stage 3a calcite is chemically distinct from magmatic calcite (Table 2). Being very pure ($CaCO_3$ component > 98 %) the hydrothermal calcite is depleted in the major additional cations, Sr, Ba and in REE (Fig. 9; Table 2). Overall, Mg, Mn and Fe, while still very low, are slightly enriched compared to the magmatic calcite (Fig. 9A; Table 2) and stage 3a calcite exhibits Mn-Fe zonation observed in SEM imaging in the intensely altered calcite carbonatite. Only yttrium does not show the intense depletion of the other REE (Fig. 9B), and is within error of the concentrations in magmatic calcite.

Stage 3 alteration involved the growth of a suite of hydrothermal minerals, including strontianite, witherite, baryte and parisite (Fig. 4B,D), and these are likely to be repositories for the elements released during hydrothermal alteration of magmatic minerals.

Parisite

Parisite is the principal REE mineral in the calcite carbonatite sample suite (average $\sum RE_2O_{3tot}$ in stage 3 parisite from the calcite carbonatite ~47 wt. %) (Fig. 7; Appendix 3). The parisite REE pattern is broadly similar to those of the magmatic phases (Fig. 7) but shows even stronger LREE enrichment than apatite.

5.3 Stage 4 alteration: REE behaviour in fluorite mineralisation

LA-ICP-MS analyses of stage 3b and stage 4 fluorite are given in Appendix 3. All fluorite generations have low concentrations of REE, with the HREE below detection except for Y, and a positive Y anomaly of a few ppm to a few hundred ppm, as is common for fluorite (Williams-Jones and Palmer, 2002; Nadoll *et al.,* 2018). Stage 4a fluorite coexists with

parisite (Fig. 5C-D) and has the highest LREE contents, averaging ∑LREE ~145 ppm; type 4c fluorite has an average ∑LREE slightly higher than type 4b fluorite (∑LREE ~ 60 ppm).

The composition of stage 4 parisite was difficult to quantify because of fine scale intergrowth with Fe-hydroxides and other phases. It apparently has a somewhat higher REE content than stage 3 parisite (average $\sum RE_2O_{3tot}$ = 58 wt. %), although this could be an artefact of the associated Fe-hydroxides. Associated stage 4 calcite has a very low LREE content (average $\sum REE_{tot(La-Nd)}$ < 40 ppm) with no detectable HREE, even though both stage 3a and stage 4 calcite coexist with parisite (Appendix 3).

5.4 Minor and trace element redistribution during hydrothermal alteration of calcite carbonatite

Primary magmatic variation:

The suite of rocks studied shows a broad increase in REE contents from mafic rocks to carbonatites. Most of the major element variations reflect the different proportion of calcite and silicate minerals (Table 4) in the different rock types. The margin of the mafic dyke (OKC4) has the lowest REE content, but all REE patterns are similar (Fig. 10). The mafic dyke core, which was subsequently intruded by calcite carbonatite, shows LREE depletion compared to the magmatic calcite carbonatites because apatite and calcite are less abundant. The mafic dyke core is also depleted in HREE, but to a lesser extent than the LREE, compared to the other calcite carbonatites. This reflects the higher total HREE content of apatite and calcite from the mafic dyke (Tables 2, 3). In contrast, the least altered diopside-bearing calcite carbonatite (OKA5) has a distinctly higher HREE content compared to other magmatic calcite carbonatites (Fig. 10; OKA1, OKC17, 18, 19-1), although no specific mineralogical host for the HREE has been identified.

Variation with hydrothermal alteration:

In order to evaluate the scale of element redistribution during hydrothermal alteration, we carried out bulk analyses on a range of relatively altered to relatively unaltered calcite carbonatites (Table 4). A simplified mass balance illustrates that for the less altered, pegmatitic calcite carbonatite (sample OKC17) there is no significant change in total REE content due to hydrothermal alteration. Calcite and apatite are respectively 95 % and 5 % of the original REE-bearing minerals in sample OKC17 (Table 4) and together made up approximately 95 % of the sample initially. Based on their ∑REE concentrations prior to hydrothermal alteration (Tables 2, 3) we can calculate the original ∑REE concentration of the rock prior to alteration as 2090 ppm. The analysed bulk ∑REE content of the sample after alteration is 2190 ppm (Table 4). These values are effectively identical within uncertainty and we conclude that, during alteration, the REE released from magmatic minerals were retained in the rock but no additional REE were added.

In contrast, a similar calculation for the more altered pegmatitic calcite carbonatite sample OKC19-1 and the intensely altered pegmatitic carbonatite sample OKC19-2, shows addition of REE. In sample OKC19-1, calcite and apatite represent respectively 95 % and 5 % of the original REE-bearing minerals, and together they made up approximately 95 % of the rock (Table 4). Based on the magmatic mineral compositions (Tables 2, 3), the ∑REE content of the original rock was 1989 ppm whereas the ∑REE of the present, altered sample is 2943 ppm (Table 4), suggesting that REE may have been added during alteration. In the intensely altered calcite carbonatite (OKC19-2), calcite and apatite represent respectively 99 % and 1 % of the original REE-bearing minerals and the sample now has approximately 18 % of added secondary silicates. No magmatic calcite remains in this sample, so we have assumed that it had the same composition as the magmatic calcite in sample OKC19-1, which was

adjacent. Assuming there were no other minerals in the original rock, the magmatic calcite and apatite compositions (Tables 2, 3) allow us to estimate an original ∑REE content of 1501 ppm for the rock prior to alteration. This is markedly lower than the ∑REE content of the present rock, which is at least 6758 ppm (Table 4, note that Ce and La values are minima). Allowing for dilution by added hydrothermal silicates, the ∑REE content of the altered carbonatite is now at least 8241 ppm, i.e. very much higher than that of the original rock. The present REE concentrations in OKC19-2 reflect the abundant parisite in this intensely altered carbonatite (Figs 4K, 10). We conclude that, although the mineralogical changes characteristic of hydrothermal alteration did not always lead to increased REE levels, the more intensely altered samples are rich in parisite and have enhanced levels of REE compared to their magmatic precursors.

Barium and strontium exhibit similar behaviour to the REE. Magmatic calcite is the main repository of Ba and Sr in the least altered rocks (Table 2), and stage 3 hydrothermal recrystallisation to a low-Ba, low-Sr calcite was accompanied by growth of Ba and Sr hydrothermal phases including baryte, witherite, strontianite and celestine. Table 4 shows that the Ba/Ca ratio of the calcite carbonatites increases with increasing degree of stage 3 alteration, with the markedly higher values for sample OKC19-2. As for the REE, the least altered samples show little evidence for enrichment in Ba, despite the appearance of barite, But there was significant enrichment in Ba in the most altered sample, OKC19-2. The true Sr concentrations of the pegmatitic calcite carbonatites are above the calibrated range of the whole rock analyses (> 10000 ppm) (Table 4), but based on the modal abundance of Sr-bearing minerals in these samples it is likely that Sr, like Ba, was also enriched during stage 3 alteration.

The enrichment in REE and Ba suggests that stage 3 alteration involves not just redistribution of minor and trace elements from magmatic minerals to hydrothermal phases on the hand specimen scale, but also some movement on a larger scale. The diopside-bearing carbonatites (OKA5 and OKA1) and pegmatitic calcite carbonatites (OKC17, 18, 19) have the same suite of stage 3 hydrothermal alteration phases and similar REE patterns (Fig. 10; Table 1). The absence of Eu and Ce anomalies from all samples are distinctive (Figs 7, 10). We infer that the most altered carbonatites accumulated trace elements through growth of secondary phases, but these may well have been released from ongoing alteration nearby (Fig. 11).

An alternative hypothesis, which merits consideration, is that these enrichments are a residual effect due to net dissolution of calcite during stage 3. However, the way in which hydrothermal calcite pseudomorphs magmatic calcite in the sample suite, and the lack of comparable enrichment in elements such as Al (Table 4), make this less likely.

In summary, stage 3 hydrothermal alteration resulted in modest changes in the composition of the calcite carbonatites, principally involving minor and trace elements which were initially present in magmatic calcite (Fig. 11). Although magmatic apatite has higher REE contents than magmatic calcite (by one order of magnitude), it is much less altered during hydrothermal alteration (< 10 %), and it is considerably less abundant than calcite, hence it released a smaller amount of REE and the major part of the REE, together with Ba and Sr for hydrothermal minerals, was derived from magmatic calcite. Nevertheless, more altered samples are enriched in Ba, Sr and REE relative to Ca, reflecting the growth of the hydrothermal stage 3 minerals in which they are concentrated, and this suggests that these elements migrated to the areas of most intense alteration on a modest scale. In contrast,

stage 4 hydrothermal alteration resulted in wholesale replacement of calcite by fluorite in the ore zones, with addition of F but removal of LREE, Ba and Sr as well as CO_2.

6. Discussion

Hydrothermal reworking has played an important role in determining the composition and mineralogy of the Okorusu carbonatite body. Hydrothermal changes are potentially significant for future exploitation of carbonatites for REE, because they dictate the REE mineralogy.

6.1 Hydrothermal reworking of the calcite carbonatites

We have argued above that the growth of parisite and other hydrothermal stage 3a phases in the calcite carbonatites resulted from breakdown of magmatic minerals, mainly calcite, releasing REE, Ba and Sr. While there is a qualitative match between the elements released from magmatic minerals and those taken up in stage 3 hydrothermal phases, the most altered samples show some enrichment, implying redistribution on a larger scale than the outcrops sampled (e.g. Fig. 3B). In particular, remobilisation gave rise to a greater local LREE enrichment in the most intensely altered calcite carbonatite (OKC19-2) reflecting abundant stage 3 parisite mineralisation (Figs 4K, 10). The most intense hydrothermal alteration of the pegmatitic calcite carbonatite pod is close to the contact with the country rock, which may reflect enhanced fluid flow at the margin of the carbonatite body (Fig. 3B).

Local LREE enrichment in the intensely altered calcite carbonatite is accompanied by accumulation of Ba and Sr, mainly as sulfates (Table 4). These are a key feature of stage 3 hydrothermal alteration at Okorusu. Since baryte and celestine are nearly insoluble (Blount, 1977; Monnin, 1999), we infer that the Ba and Sr released from the breakdown of magmatic calcite and apatite were fixed by interaction with sulfate. A small percentage of magmatic

pyrite (< 5 %) was present in the calcite carbonatites initially, but is now partially altered to Fe-hydroxides (Fig 4G) and so the reaction of pyrite with an introduced hydrothermal fluid is a likely source of local sulfate (Fig. 11).

The stage 3 fluid is inferred to have been oxidising because of the production of sulfate and the association of Fe-hydroxides with the stage 3b assemblages, however it was not sufficiently oxidising for Ce to be fractionated from the rest of the REE as Ce^{4+}, as described in a similar setting by Anenburg *et al.,* (2018b). Assuming that all the Ba and Sr in the intensely altered calcite carbonatite (OKC19-2) are present in sulfate minerals, approximately 13000 ppm of sulfur was needed to fix them. Oxidation of 3 % modal pyrite, a typical level for the magmatic calcite carbonatites, will release around 16000 ppm sulfur as sulfate and so it is likely that sufficient sulfur is available in-situ to fix the elevated Ba and Sr levels present in this sample.

There was probably an excess of Ba and Sr available, since they also form carbonate minerals, and in this case sulfate would not have been available in solution to enhance REE mobility (Migdisov and Williams-Jones, 2008).

6.2 Conditions of REE mineralisation and hydrothermal reworking

By analogy to experimental work on carbonatite systems by Weidendorfer *et al.,* (2017) it is likely that the temperature of the magmatic stage of the Okorusu carbonatites was between 700 °C and 1050 °C, although late-magmatic stage 2 crystallisation may have been somewhat cooler. Bühn *et al.,* (2002) estimated that stage 4 alteration and fluorite growth took place at 150 °C ± 30 °C from fluid inclusion studies. Stage 3 and stage 4 hydrothermal alterations result in a similar hydrothermal mineral suite, although stage 4 is dominated by fluorite. In particular, calcite is present coexisting with dolomite in both stage 3 and stage 4.

The Mg content of calcite coexisting with dolomite is the basis for the calcite-dolomite solvus geothermometer calibrated by Anovitz and Essene (1987). In practice, the Mg content of stage 3a and stage 4 calcite is too low (XMg < 0.001, Table 2) to apply this geothermometer except to give an upper temperature limit. The data indicate that both stages 3 and 4 developed at temperatures < 200 °C, in agreement with the earlier fluid inclusion results.

6.3 The relation between carbonatite evolution and hydrothermal reworking

High-temperature hydrothermal activity commonly affects the rocks around carbonatite complexes, notably through the formation of fenites (Zharikov *et al.,* 2007, Elliott et al 2018), and so it is reasonable to ask if such magmatic fluids played a role in the hydrothermal alteration described here. Carbonatite melts are low viscosity (Jones *et al.,* 2013) and rich in chloride salts and volatiles, predominantly CO_2 and H_2O (Mitchell, 2005; Rankin 2005). Salts and volatiles which are not retained in the carbonatite rocks give rise to fenitizing fluid (Elliott *et al.,* 2018). A minimum fenitization temperature of 500 °C ± 30 °C is indicated by experimental work (Zaraiskii, 1989). The upper temperature limit of fenites in natural systems is > 700 °C, measured at Amba Dongar (Williams-jones and Palmer, 2002). These are very different from the conditions of the hydrothermal alteration observed at Okorusu (Table 1), which indicate a distinct break between magmatic and hydrothermal conditions. In the absence of evidence of high-T alteration in the studied rocks it unlikely that late stage magmatic fluids were the only source responsible (c.f. Trofanenko *et al.,* 2016). Furthermore, the fluid inclusions hosted in the fluorite lack a CO_2 component and show low salinities (Bühn *et al.*, 2002), unlike carbonatite fluid inclusions observed in other carbonatite bodies (e.g. Shu and Liu, 2019; Zheng and Liu, 2019; Rankin, 2005). Instead, the alteration observed is consistent with a maximum temperature of 200 °C and the oxidising

character of the hydrothermal fluid is suggestive of a geothermal system involving surface waters, although a magmatic origin for the added F seems very likely. A link between geothermal systems and hydrothermal mineralisation is widely documented from many settings, with water of meteoric origin interacting with components derived from magmatic fluids and gases to produce a wide range of epithermal ores (e.g. White, 1981; Krupp and Seward, 1987). In this example, the development of hydrothermal massive fluorite points to continued magmatic vapor contributions to the geothermal fluid system down to low temperatures (Bühn *et al.*, 2002, 2003).

7. Conclusions

The REE-rich carbonatites at Okorusu are originally of magmatic origin, but hydrothermal reworking has served to redistribute the REE into new minerals. Three alteration stages redistributed the REE at Okorusu. Stage 2 mineral growth is late magmatic and results in minor growth of REE-depleted apatites after magmatic (stage 1) apatite. Stage 2 apatites exhibit lower REE contents than the stage 1 grains across the full lanthanide series (Fig. 7) but were accompanied by cogenetic parisite. Stages 3 and 4 are two distinct low temperature hydrothermal events. Stage 3 involves partial breakdown of apatite and extensive recrystallisation of more abundant, trace element-rich magmatic calcite, to purer hydrothermal calcite. Elements released from stage 1 magmatic minerals during alteration precipitated as parisite, baryte and celestine with lesser amounts of strontianite, witherite and other minor phases. Overall, stage 3 alteration is widespread in the different carbonatite pods and dykes, and is dominated by redistribution of REE without significant change in the bulk rock composition. Nevertheless, there is evidence of enrichment in Sr, Ba and REE during alteration in the most altered calcite carbonatites (Fig. 11). In contrast, stage

4 alteration resulted in widespread replacement of calcite carbonatite bodies (including those affected by stage 2 and stage 3 alteration) and country rock marbles by fluorite, and is accompanied by much more extensive metasomatic change than stage 3. Fluorite ore is low in Ba, Sr and REE irrespective of precursor lithology and only the earliest fluorite, type 4a, has associated parisite. The REE profiles of minerals from all alteration stages are close to that of the main REE-bearing magmatic phases (Fig. 7). Likewise, the REE bulk rock patterns of the different rocks (from mafic to fluorite ore) are comparable (Fig. 10). This suggests that the REE-bearing minerals developed in stages 2, 3 and 4 formed by redistribution of the REE from stage 1 magmatic minerals without a major external source of REE (Fig. 11).

Stage 3 alteration is responsible for the most abundant REE mineralisation at Okorusu, with REE derived from magmatic phases being concentrated into hydrothermal parisite. It developed at a temperature less than 200 °C and the associated baryte and celestine indicate an oxidising hydrothermal fluid, with sulfate likely derived from oxidation of magmatic pyrite. The most altered calcite carbonatite (OKC19-2) appears to have been enriched in Ba, Sr and REE during the alteration.

The stage 3 and stage 4 hydrothermal alteration at Okorusu developed under low temperature, mildly oxidising conditions typically associated with geothermal systems. It is likely that surface-derived waters played an important role, but the extensive development of fluorite in stage 4 is indicative of an important contribution of F-rich fluid, likely of magmatic origin (Bühn *et al.*, 2002, 2003).

Although Okorusu does not have economic potential for REE at present, this study demonstrates that hydrothermal alteration can serve to concentrate REE, forming hydrothermal REE minerals. The hydrothermal alteration of the main magmatic gangue

mineral at Okorusu (calcite) has proven to be able to concentrate a significant amount of REE to form parisite-rich areas. Small amounts of hydrothermal alterations are sufficient to facilitate recrystallisation and the accompanying concentration of trace and minor elements into their own discrete secondary minerals, but more extensive alteration appears to be necessary to achieve significant overall enrichment.

Acknowledgements

We would like to thank Richard Walshaw and Duncan Hedges for help with the SEM imaging and the EPMA analyses at the University of Leeds. Ed Loye (University of Exeter) for organising access to Okorusu mine and Pedro and Boni for guiding us in the field at Okorusu. Rainer Ellmies (Gecko Namibia) kindly gave permission for the reproduction of the 3D mine model in Fig. 2. The manuscript was greatly improved by the contributions of 3 anonymous referees, while an earlier version benefitted from the perceptive comments of Dr. Chakhmouradian and Dr. Jindrich Kynicky.

Funding

This work was supported by the NERC SOS:RARE project (NE/M01147X/1).

References

Alderton, D.H.M., Pearce, J.A. and Potts, P.J. (1980) Rare earth element mobility during granite alteration: evidence from the southwest England. *Earth and Planetary Science Letters,* **49**, 149-165.

Anenburg, M., and Mavrogenes, J.A. (2018a) Carbonatitic versus hydrothermal origin for fluorapatite REE-Th deposits: Experimental study of REE transport and crustal "antiskarn" metasomatism. *American Journal of Science*, **318**, 335-366.

Anenburg, M., Burnham, A.D. and Mavrogenes, J.A. (2018b) Ree redistribution textures in altered fluorapatite: Symplectites, veins, and phosphate-silicate-carbonate assemblages from the Nolans bore p-ree-th deposit, Northern Territory, Australia. *Canadian Mineralogist*, **56**(3), 331-354.

Anovitz, L.M. and Essene, E.J. (1987) Phase equilibria in the system $CaCO_3$-$MgCO_3$-$FeCO_3$. *Journal of Petrology,* **28**, 389-414.

Banks, D.A., Yardley, B.W.D., Campbell, A.R. and Jarvis, K.E. (1994) REE composition of an aqueous magmatic fluid: A fluid inclusion study from the Capitan Pluton, New Mexico, U.S.A. *Chemical Geology*, **113**, 259-272.

Belousova, E.A., Griffin, W.L., O'Reilly, S.Y., and Fisher, N.I. (2002) Apatite as an indicator mineral for mineral exploration: trace-element compositions and their relationship to host rock type. *Journal of Geochemical Exploration*, **76**, 45-69.

Blount, C. (1977) Baryte solubilities and thermodynamic quantities up to 300°C and 1400 bars. *American Mineralogist,* **62**, 942-957.

Broom-Fendley, S., Styles, M.T., Appleton, J.D., Gunn, G. and Wall, F. (2016) Evidence for dissolution-reprecipitation of apatite and preferential LREE mobility in carbonatite-derived late-stage hydrothermal processes. *American Mineralogist*, **101**, 596-611.

Broom-Fendley, S., Aoife, B.E., Wall, F., Gunn, G. and Dawes, W. (2017a) REE minerals at the Songwe Hill carbonatite, Malawi: HREE-enrichment in late-stage apatite. *Ore Geology Reviews,* **81**, 23-41.

Broom-Fendley, S., Wall, F., Spiro, B. and Ullmann, C.V. (2017b) Deducing the source and composition of rare earth mineralising fluids in carbonatites: insights from isotopic (C, O,

$^{87}Sr/^{86}Sr$) data from Kangankunde, Malawi. *Contributions to Mineralogy and Petrology*, **172**, 96.

Bühn, B., Rankin, A.H., Schneider, J. and Dulski, P. (2002) The nature of orthomagmatic, carbonatitic fluids precipitating REE, Sr-rich fluorite: fluid-inclusion evidence from the Okorusu fluorite deposit, Namibia. *Chemical Geology,* **186**, 75-98.

Bühn, B., Schneider, J., Dulski, P. and Rankin, A.H. (2003) Fluid-rock interaction during progressive migration of carbonatitic fluids, derived from small-scale trace element and Sr, Pb isotope distribution in hydrothermal fluorite. *Geochimica et Cosmochimica Acta*, **67**, 4577-4595.

Chakhmouradian, A.R., Reguir, E.P. and Zaitsev, A.N. (2016) Calcite and dolomite in intrusive carbonatites. I. Textural variations. *Mineralogy and Petrology*, **110**, 333-360.

Chakhmouradian, A.R., Reguir, E.P., Zaitsev, A.N., Couëslan, C., Xu, C., Kynický, J., Mumin, A.H. and Yang, P. (2017) Apatite in carbonatitic rocks : Compositional variation, zoning, element partitioning and petrogenetic significance. *Lithos*, **275**, 188-213.

Chakhmouradian, A.R. and Wall, F. (2012) Rare earth elements: Minerals, mines, magnets (and more). *Elements*, **8**, 333-340.

Chakhmouradian, A.R. and Zaitsev, A.N. (2012) Rare earth mineralization in igneous rocks: Sources and processes. *Elements*, **8**, 347-353.

Chebotarev, D.A., Veksler, I.V., Wohlgemuth-Ueberwasser, C., Doroshkevich, A.G., and Koch-Müller, M. (2019) Experimental study of trace element distribution between calcite, fluorite and carbonatitic melt in the system $CaCO_3 + CaF_2 + Na_2CO_3 \pm Ca_3(PO_4)_2$ at 100 MPa. *Contributions to Mineralogy and Petrology*, **174**(1), 1-13.

Elliott, H.A.L., Wall, F., Chakhmouradian, A.R., Siegfried, P.R., Dahlgren, S., Weatherley, S., Finch, A.A., Marks, M.A.W., Dowman, E., and Deady, E. (2018) Fenites associated with carbonatite complexes: A review. *Ore Geology Reviews*, **93**, 38-59.

European Commission (2017) Communication from the commission to the European parliament, the council. *The European economic and social committee and the committee of the regions on the 2017 list of Critical Raw Materials for the EU*. COM(2017) 490.

Feng, M. Xu, C., Kynicky, J., Zeng, L. and Song, W. (2016) Rare earth element enrichment in Palaeoproterozoic Fengzhen carbonatite from the North China block. *International Geology Review*, **58**(15) 1940-1950.

Giebel, R.J., Gauert, C.D.K., Marks, M.A.W., Costin, G. and Markl, G. (2017) Multi-stage formation of REE minerals in the Palabora Carbonatite Complex, South Africa. *American Mineralogist,* **102**, 1218-1233.

Glover, E.D. and Sippel, R.F. (1962) Experimental pseudomorphs: Replacement of calcite by fluorite. *American Mineralogist,* **47**, 1156-1165.

Gysi, A.P. and Williams-Jones, A. (2013) Hydrothermal mobilization of pegmatite-hosted REE and Zr at Strange Lake, Canada: a reaction path model. *Geochimica et Cosmochimica Acta,* **122**, 324-352.

Hagni, R.D. and Shivdasan, P.A. (2000) Characterizing megascopic textures in flurospar ores at Okorusu mine. *Microtextural Mineralogy*, 17-19.

Hagni, R.D. and Shivdasan, P.A. (2001) Application of cathodoluminescence microscopy to the study of carbonatite-related fluorspar ores, host rock carbonatites and beneficiation products at Okorusu, Namibia. *Minerals and Metallurgical Processing*, **18**(4), 203-208.

Harlov, D.E., Förster, H.J., and Schmidt, C. (2003) High P-T experimental metasomatism of a fluorapatite with significant britholite and fluorellestadite components: implications for LREE mobility during granulite-facies metamorphism. *Mineralogical Magazine*, **67**, 61-72.

Harlov, D.E., Wirth, R. and Förster, H.J. (2005) An experimental study of dissolution-reprecipitation in fluorapatite: Fluid infiltration and the formation of monazite. *Contributions to Mineralogy and Petrology*, **150**(3), 268-286.

Holtstam, D. and Andersson, U.B. (2007). The REE minerals of the Bastnäs-type deposits, South-Central Sweden. *Canadian Mineralogist*, **45**, 1073-1114.

Holtstam, D., Andersson, U.B., Broman, C. and Mansfeld, J. (2014) Origin of REE mineralization in the Bastnäs-type Fe–REE-(Cu–Mo–bi–Au) deposits, Bergslagen, Sweden. *Mineralium Deposita*, **49**, 933-966.

Jones, A.J., Genge, M. and Carmody, L. (2013) Carbonate melts and carbonatites. *Reviews in Mineralogy and Geochemistry*, **75,** 289-322**.**

Kapustin, I. (1980) *Mineralogy of carbonatites*. Amerind Publ Co, New Delhi.

Krupp, R.E. and Seward, T.M. (1987) The Rotokawa geothermal system, New Zealand: An active epithermal gold-depositing environment. *Economic Geology*, **82**, 1109-1129.

Le Bas, M.J. and Srivastava, R.K. (1989) The mineralogy and geochemistry of the Mundwana carbonatite dykes, Sirohi District, Rajasthan, India. *Journal of Mineralogy and Geochemistry*, **160**, 207-227.

Lewis, A.J., Komninou, A., Yardley, B.W.D. and Palmer, M.R. (1998) Rare earth element speciation in geothermal fluids from Yellowstone National Park, Wyoming, USA. *Geochimica et Cosmochimica*, **62**, 657-663.

Linnen, R.L., Samson, I.M., Williams-Jones, A.E. and Chakhmouradian, A.R. (2014) Geochemistry of the rare-earth element, Nb, Ta, Hf, and Zr deposits. Pp 543-569 in: *Treatise on Geochemistry*: Second Edition, Elsevier

McDonough, W.F. and Sun, S. (1995) The composition of the earth. *Chemical Geology,* **120**, 223-253.

Migdisov, A., Williams-Jones, A.E., Brugger, J. and Caporuscio, F.A. (2016) Hydrothermal transport, deposition, and fractionation of the REE: Experimental data and thermodynamic calculations. *Chemical Geology,* **439**, 13-42.

Migdisov, A.A. and Williams-Jones, A.E. (2008) A spectrophotometric study of Nd(III), Sm(III) and Er(III) complexation in sulfate-bearing solutions at elevated temperatures. *Geochimica et Cosmochimica Acta,* **72**, 5291-5303.

Milner, S.C., Le Roex, A.P. and O'Connor, J.M. (1995) Age of Mesozoic igneous rocks in northwestern Namibia, and their relationship to continental breakup. *Journal of the Geological Society*, **152**, 97-104.

Mitchell, R.H. (2005) Carbonatites and carbonatites and carbonatites. *Canadian Mineralogist*, **43**, 2049-2068.

Monnin, C. (1999) A thermodynamic model for the solubility of barite and celestine in electrolyte solutions and seawater to 200°C and to 1 kbar. *Chemical Geology*, **153**, 187-209.

Moore, M., Chakhmouradian, A.R., Mariano, A.N. and Sidhu, R. (2015) Evolution of rare-earth mineralization in the Bear Lodge carbonatite, Wyoming: Mineralogical and isotopic evidence. *Ore Geology Reviews,* **64**, 499-521.

Nadoll, P. Rehm, M., Duschl, F., Klemd, R., Kraemer, D., and Sośnicka, M. (2018) REY and

trace element chemistry of fluorite from Post-Variscan hydrothermal veins in Paleozoic units of the North German Basin. *Geosciences*, **8**(8), 283-312.

Packwood, R.H. and Brown, J.D. (1981) A Gaussian expression to describe Φ(ρz) curves for quantitative electron probe microanalysis. *X-RAY Spectrometry,* **10**, 138-146.

Perry, P. and Gysi, A. (2018) Rare earth elements in mineral deposits: speciation in hydrothermal fluids and partitioning in calcite. *Geofluids, **2018***, 1-19.

Rankin, A.H. (2005) Carbonatite-associated rare metal deposits—Composition and evolution of ore-forming fluids-The fluid inclusion evidence. pp. 299-314 in: Rare-element geochemistry and mineral deposits (Linnen, R.L. and Samson, I.M. editors) Quebec: Geological Association of Canada, Short Course Notes 17.

Reguir, E.P. Chakhmouradian, A.R., Pisiak, L.H., Halden,N.M., Yanng, P. Xu, C., Kynický, J. and Couëslan, C.G. (2012) Trace-element composition and zoning in clinopyroxene- and amphibole-group minerals: Implications for element partitioning and evolution of carbonatites. *Lithos*, **128-131**, 27-45.

Roedder, E. (1973) Fluid inclusions from the fluorite deposits associated with carbonatite of Amber Dongar, India and Okorusu, South West Africa. *Transaction of the Institution of Mining and Metallurgy*, **82**, 35-39.

Schreiber, U.M., Minlners, S.C. and Goscombe, B.G. (1977) Geological map of Namibia: 1:250 000 geological series.

Shivdasan, P. (2002) *Petrology, geochemistry, and mineralogy of pyroxene and pegmatite carbonatite and the associated fluorspar deposit at Okorusu alkaline igneous carbonatite complex, Namibia*. PhD dissertation, University of Missouri-Rolla, USA.

Shu, X. and Liu, Y. (2019) Fluid inclusion constraints on the hydrothermal evolution of the Dalucao Carbonatite-related REE deposit, Sichuan Province, China. *Ore Geology Reviews*, **107**, 41-57.

Smith, M.P., Henderson, P. and Campbell, L.S. (2000) Fractionation of the REE during hydrothermal processes: constraints from the Bayan Obo Fe-REE-Nb deposit, Inner Mongolia, China. *Geochimica et Cosmochimica Acta,* **64**, 3141-3160.

Smith, M.P., Moore, K., Finch, A.A., Kynicky, J. and Wall, F. (2016) From mantle to critical zone, a review of large and giant sized deposits of the rare earth elements. *Geoscience Frontiers,* **7**, 315-334.

Sturm, R. (2002) PX-NOM - An interactive spreadsheet program for the computation of pyroxene analyses derived from the electron microprobe. *Computers and Geosciences*, **28**, 473-483.

Trofanenko, J., Williams-Jones, A.E., Simandl, G.J. and Migdisov, A.A. (2016) The nature and origin of the REE mineralization in the Wicheeda carbonatite, British Columbia, Canada. *Economic Geology,* **111**, 199-223.

U.S. Geological Survey (2018) Mineral commodity summaries 2018, U.S. *Geological Survey*, 1-204.

Van Zijl, P (1962) *The geology, structure and petrology of the alkaline intrusions of Kalkfeld and Okorusu and the invaded Damara rocks*. PhD dissertation, University of Stellenbosch, South Africa.

Verplanck, P.L., Mariano, A.N. and Mariano, A. (2016) Rare earth element ore geology of carbonatites. pp. 5-32 in: *Rare earth and critical elements in ore deposits* (Hitzman, M.W. editors. Review of Economic Geology*,* **18**.

Wall, F., Niku-Paavola, V.N., Storey, C.M. and Axel, J.T. (2008) Xenotime-(Y) from carbonatite dykes at Lofdal, Namibia: Unusually low LREE:HREE ratio in carbonatite, and the first dating of xenotime overgrowths on zircon. *Canadian Mineralogist,* **46**, 861-877.

Wall, F. (2014) Rare Earth Elements. pp. 312-340 in: *Critical Metals Handbook* (Gunn, A. editor). Wiley, New York, USA.

Weidendorfer, D., Schmidt, M.W. and Mattsson, H.B. (2017) A common origin of carbonatite magmas. *Geology*, **45**(6), 507-510.

White, D.E. (1981) Active geothermal systems and hydrothermal ore deposits. *Economic Geology*, **75**, 392-423.

Williams-Jones, A.E. and Palmer, D.A.S. (2002) The evolution of aqueous-carbonic fluids in the Amba Dongar carbonatite, India: Implications for fenitisation. *Chemical Geology*, **185**, 283-301.

Williams-Jones, A.E., Migdisov, A.A. and Samson, I.M. (2012) Hydrothermal mobilisation of the rare earth elements-a tale of “ceria” and “yttria”’. *Elements,* **8**, 13-42.

Zaitsev, A.N., Wall, F. and Le Bas, M.J. (1998) REE-Sr-Ba minerals from the Khibina carbonatites, Kola Peninsula, Russia: their mineralogy, paragenesis and evolution. *Mineralogical Magazine*, **62**, 225-250.

Zaitsev, A., Demény, A., Sindern, S. and Wall, F. (2002) Burbankite group minerals and their alteration in rare earth carbonatites: source of elements and fluids (evidence from C-O and Sr-Nd isotopic data). *Lithos,* **62**, 15-33.

Zaraiskii, G.P. (1989) Zonation and Conditions of Metasomatic Rocks Formation. Nauka Publishing, Moscow.

Zharikov, V.A., Pertsev, N.N., Rusinov, V.L., Callegari, E., Fettes, D.J. (2007) Metasomatism and metasomatic rocks. In: Recommendations by the IUGS Subcommision of the Systematics of Metamorphic Rocks. British Geological Survey.

Zheng, X. and Liu, Y. (2019) Mechanisms of element precipitation in carbonatite-related rare-earth element deposits: Evidence from fluid inclusions in the Maoniuping deposit, Sichuan Province, southwestern China. *Ore Geology Reviews*, **107**, 218-238.

Figure captions

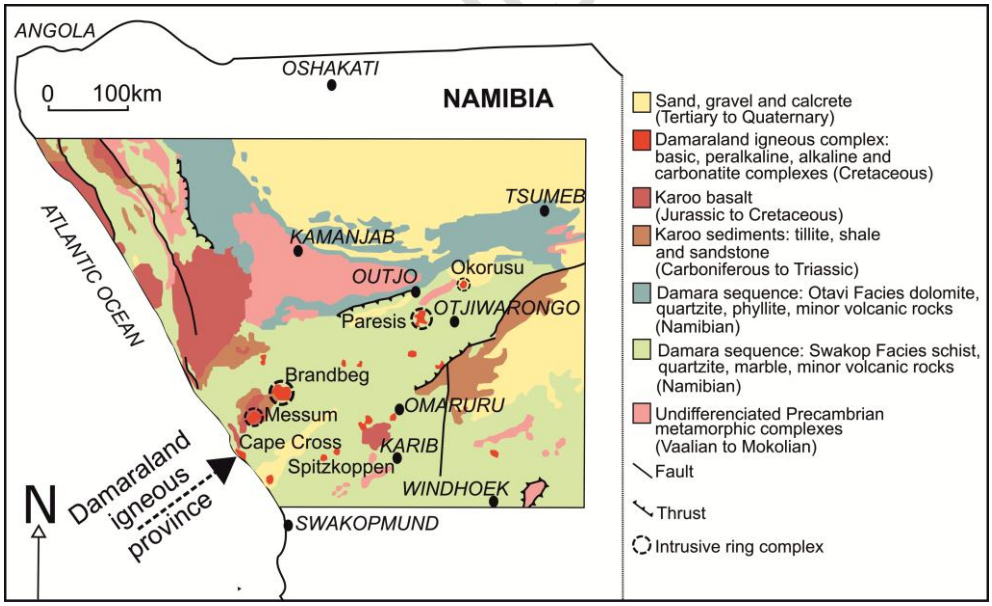

FIG. 1. Simplified geological map of Namibia showing the Damaraland igneous province trending North-East (after the geological map of Namibia, from Schreiber et al., 1977).

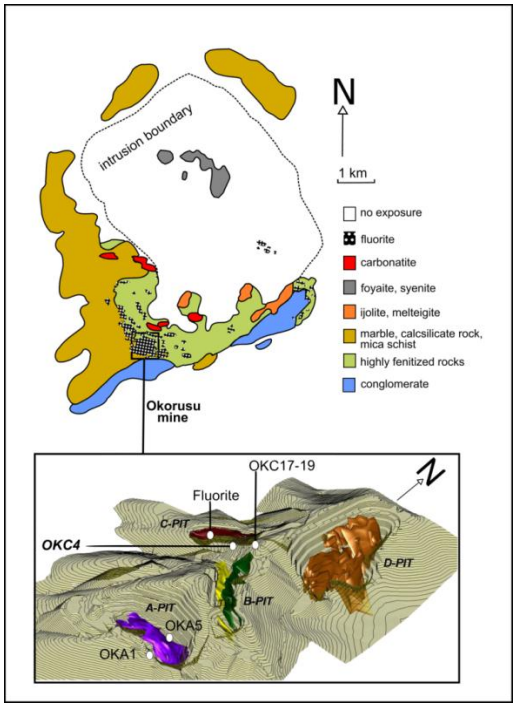

FIG. 2. Simplified geology of the Okorusu carbonatite complex (after Van Zijl, 1962) with a 3D model of the Okorusu fluorite mine and the locations of samples used in this study (the fluorite ore bodies are represented in different colours only to differentiate fluorite in different pits) (Okorusu Fluorspar, 2014, personal communication).

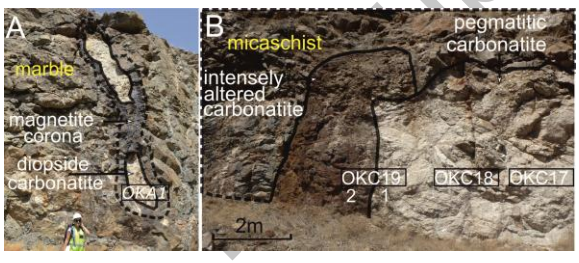

FIG. 3. Field relationships at the sample sites. Note that 'calcite' from calcite carbonatite was omitted in the figure (A) OKA1 altered diopside-bearing calcite carbonatite occurs as two elongated pods with a magnetite aureole. (B) Pegmatitic calcite carbonatite pod with highly altered margin referred to the intensely altered calcite carbonatite (OKC19-2). Samples OKC17 was taken from the middle of the pod, sample OKC19 at the contact with the altered margin.

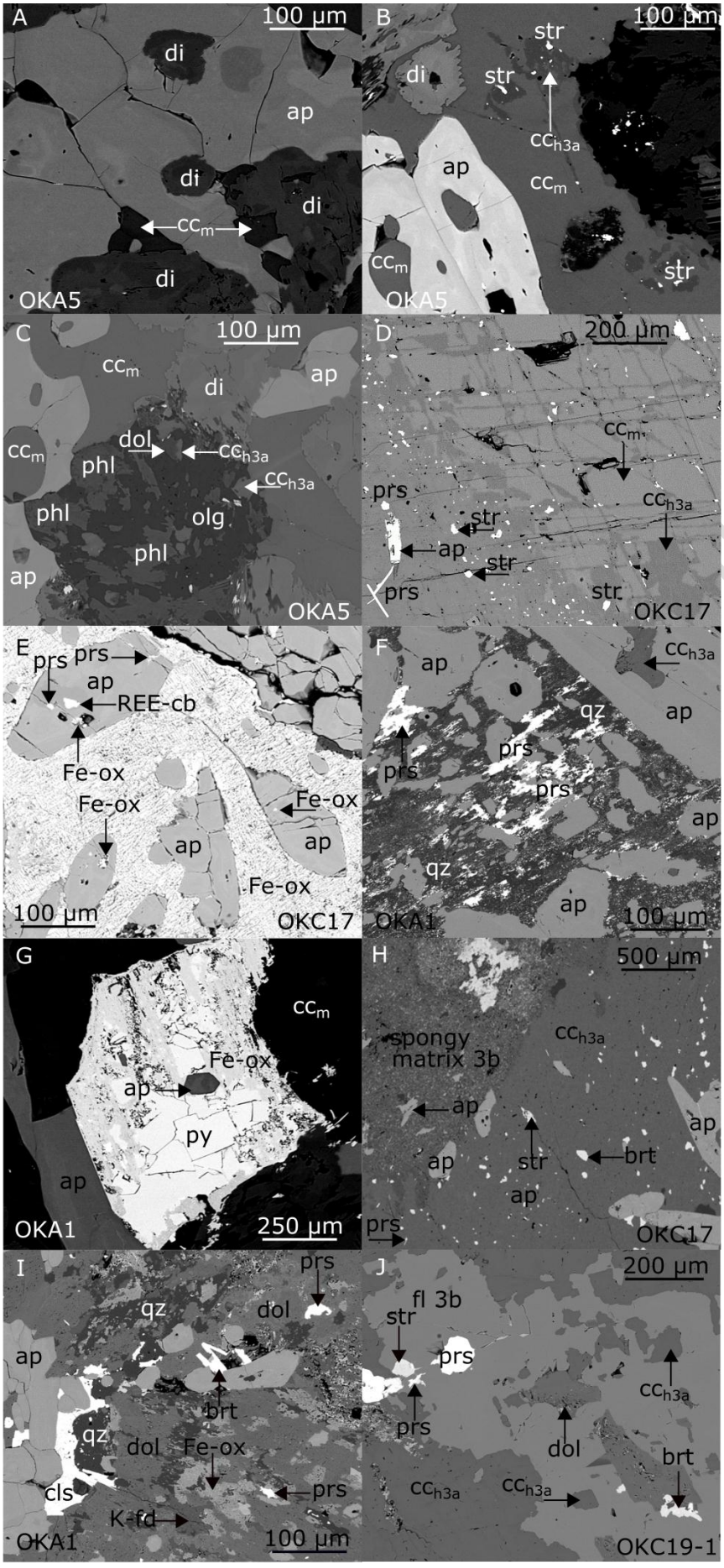
A
100 µm
di
ap
di
di
cc_m
di
OKA5
B
100 µm
str
di
str
cc_{h3a}
ap
cc_m
cc_m
str
OKA5
C
100 µm
cc_m
di
ap
cc_m
dol
cc_{h3a}
phl
cc_{h3a}
phl
olg
phl
ap
OKA5
D
200 µm
cc_m
prs
cc_{h3a}
str
ap
str
prs
str
OKC17
E
prs
prs
ap
REE-cb
Fe-ox
Fe-ox
Fe-ox
ap
ap
Fe-ox
100 µm
OKC17
F
ap
cc_{h3a}
qz
ap
prs
prs
prs
ap
qz
ap
OKA1
100 µm
G
cc_m
Fe-ox
ap
py
ap
OKA1
250 µm
H
500 µm
spongy
matrix 3b
cc_{h3a}
ap
ap
ap
str
brt
ap
prs
OKC17
I
prs
qz
dol
ap
brt
qz
dol
Fe-ox
cls
prs
K-fd
OKA1
100 µm
J
200 µm
fl 3b
str
prs
cc_{h3a}
prs
dol
brt
cc_{h3a}
cc_{h3a}
OKC19-1

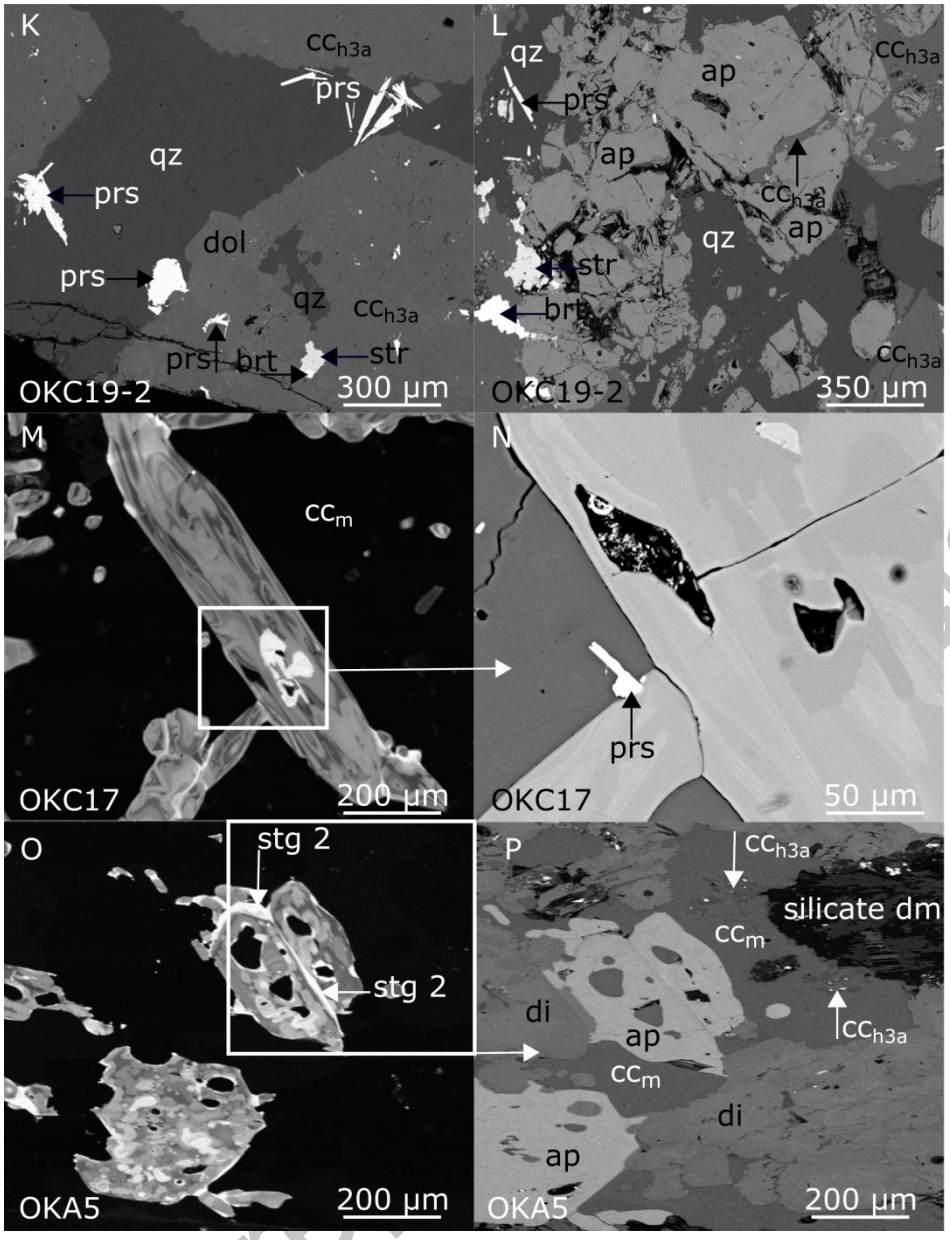

FIG. 4. Back scattered electron (BSE) (image A to L + N + P) and cathodoluminescence (CL) (image M + O) images of magmatic and hydrothermal alteration textures of the Okorusu calcite carbonatites. (A) Sample OKA5 showing early diopside displaying irregular zoning with corroded crystal edge enclosed in later magmatic apatite; (B) Sample OKA5 with magmatic calcite forming rounded inclusions in apatite, early corroded diopside enclosed in magmatic calcite and hydrothermal calcite (dark grey-stage 3a) containing strontianite inclusions; (C) Sample OKA5 with a silicate domain of intergrown plagioclase and phlogopite; (D) Sample OKC17 showing magmatic calcite replaced along cleavage planes by

hydrothermal calcite, strontianite and parisite (stage 3a); (E) Sample OKC17 with subhedral to euhedral apatite enclosed in iron hydroxide with parisite and other alteration minerals along the apatite fractures. (F) Sample OKA1 with variably replaced magmatic apatites in a quartz matrix; parisite occurs as fine grains in the matrix and as replacement of apatite; (G) Sample OKA1 with partially oxidised pyrite and euhedral apatite inclusion; (H) Sample OKC17 showing recrystallised calcite (stage 3a), strontianite and baryte inclusions, corroded by a spongy assemblage (stage 3b), magmatic apatite occurs in both hydrothermal assemblages; (I) Sample OKA1 with magmatic apatite in extensively recrystallised matrix (stage 3a) consisting of dolomite, iron hydroxide, K-feldspar, quartz, celestine, baryte and parisite; (J) Sample OKC19-1 with stage 3b fluorite partially replacing stage 3a calcite; (K) Sample OKC19-2 with coarse euhedral parisite intergrown with stage 3a quartz and calcite; (L) Sample OKC19-2 with relict of igneous apatite fractured by stage 3a calcite associated with quartz, strontianite, baryte and parisite mineralisation; (M) SEM-CL image of apatite in sample OKC17. Stage 1 apatite exhibits complex zoning in lower intensity greys while stage 2 apatite is the distinctive bright material on rims, in late cracks and in an irregular central pore-filling; (N) BSE image of the area shown in M, with a euhedral parisite embedded at the edge of the apatite, note that the stage 2 apatite corresponds here to the darkest zone, (O) SEM-CL image of apatite in sample OKA5 showing stage 2 apatite; (P) BSE image of the area shown in (O) showing that stage 1 and 2 are enclosed in magmatic calcite. Abbreviations: cc_m*–magmatic calcite;* cc_{h3a} *–hydrothermal calcite; di—diopside; ap—apatite; str—strontianite; phl—phlogopite; olg—oligoclase; dol—dolomite; prs—parisite; REE-cb—REE-carbonate; Fe-ox—unidentified Fe- hydroxide; qz—quartz; py—pyrite; brt—baryte; K-fd—K-feldspar; cls—celestine; fl—fluorite, stg 2—stage 2 apatite; silicate dm—silicate domain.*

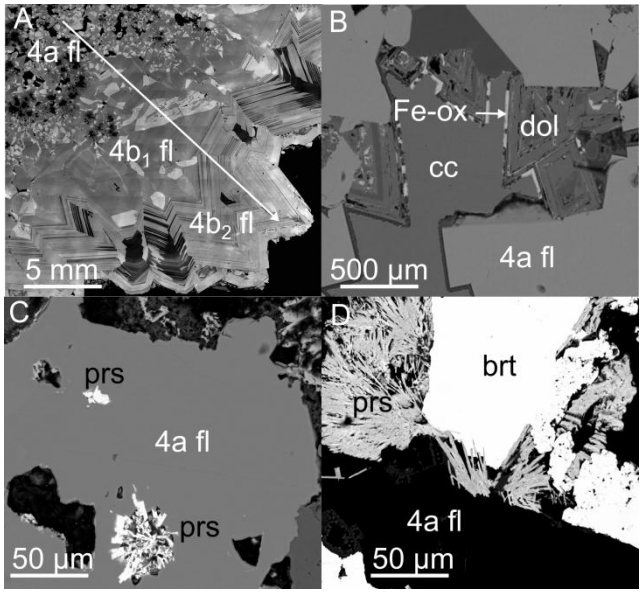

FIG. 5. CL and BSE images illustrating stage 4 textures (sample OKC6, OKC3 and OKC8). (A) SEM-CL image showing the sequential crystallisation represented by the arrow of type 4a and type 4b fluorite; (B) BSE image demonstrating the sequential crystallisation of type 4a fluorite, quartz, dolomite, iron hydroxide and stage 4 calcite, note that the Fe and Mg content of dolomite varies; (C) BSE image of parisite mineralisation embedded in a cavity lining in type 4a fluorite; (D) BSE image of radiating parisite crystals growing into baryte in type 4a fluorite.

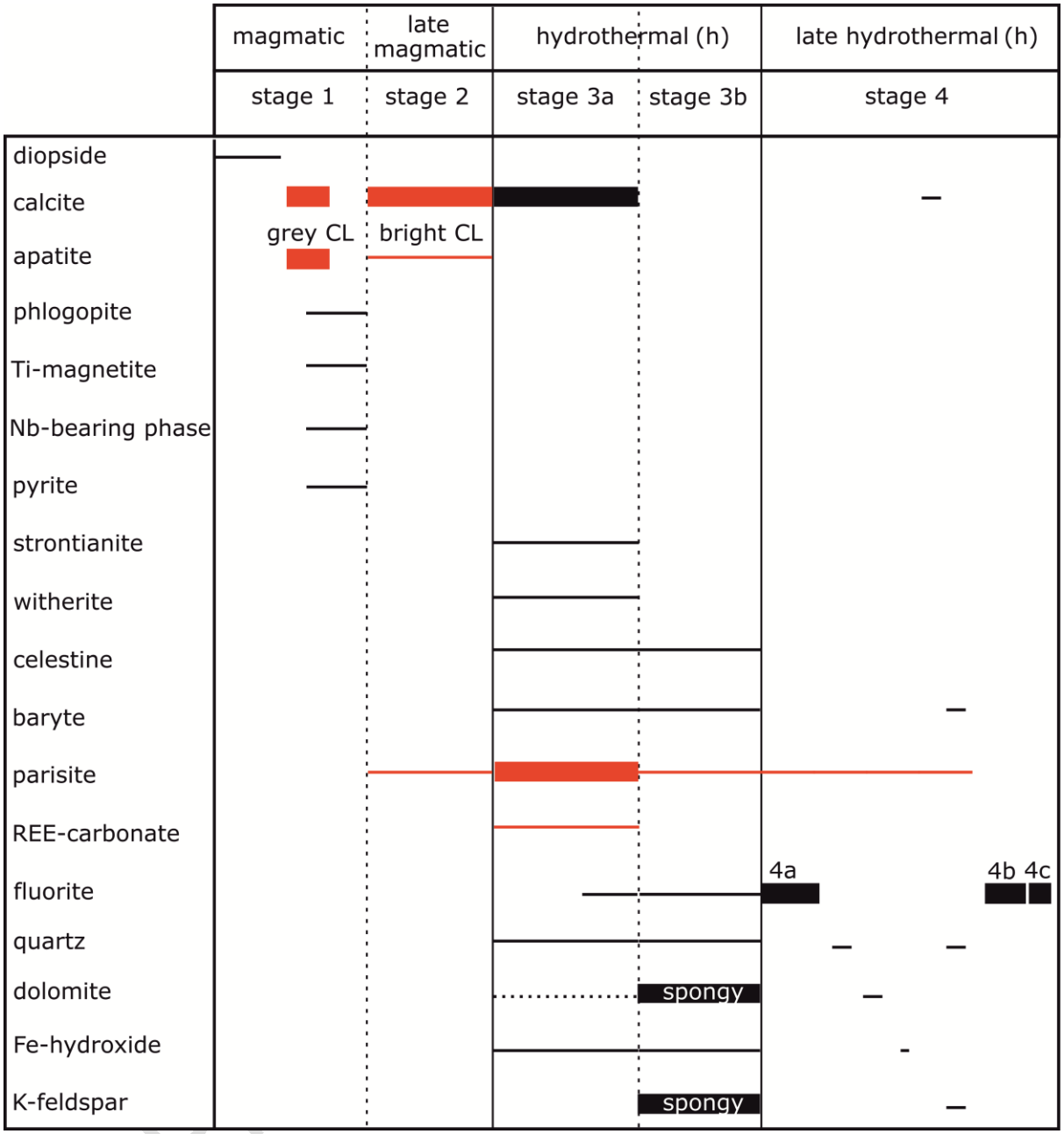

FIG. 6. Simplified paragenetic diagram of the Okorusu carbonatite deposit illustrating the REE reworking from magmatic (associated to gangue minerals) to hydrothermal as REE minerals. Bar thickness represents mineral abundance. Red bars represent the main REE-bearing minerals in each stage. Abbreviation: late m– late magmatic.

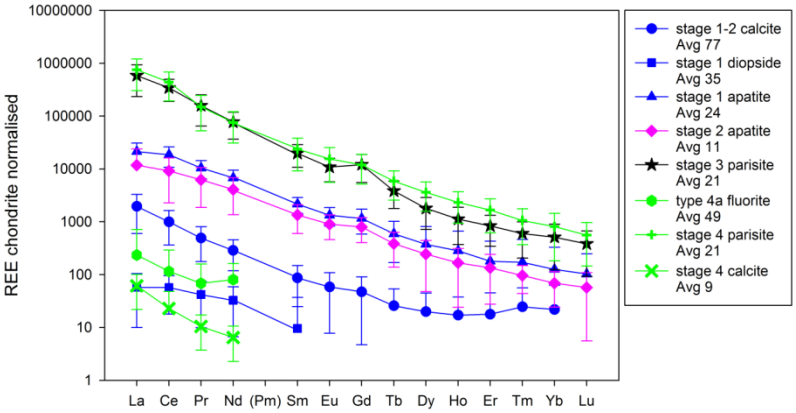

FIG. 7. REE distribution of the REE-bearing minerals observed in magmatic stages 1 and 2 (blue, pink) and hydrothermal stages 3 and 4 (black and green). Type 3b and 4c fluorite are omitted due to their low REE content (Appendix 3). Data are chondrite normalised (McDonough and Sun, 1995)*. Data from EPMA and LA-ICP-MS analyses, error bars represent two standard deviations of the average value, some of the error bars are not visible due to the y-axis log scale.*

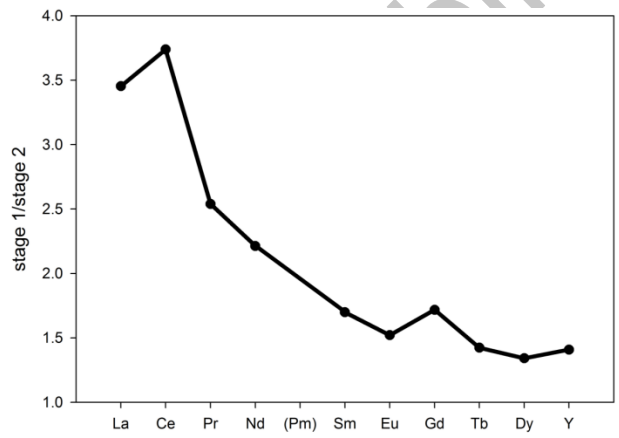

FIG. 8. Ratio of REE concentration in stage 1 vs stage 2 apatite of sample OKC19-2, stage 1 apatite n = 12 and stage 2 apatite n = 6. Ho-Lu were omitted due to the low concentration (< 30 ppm) of these elements in both apatite types.

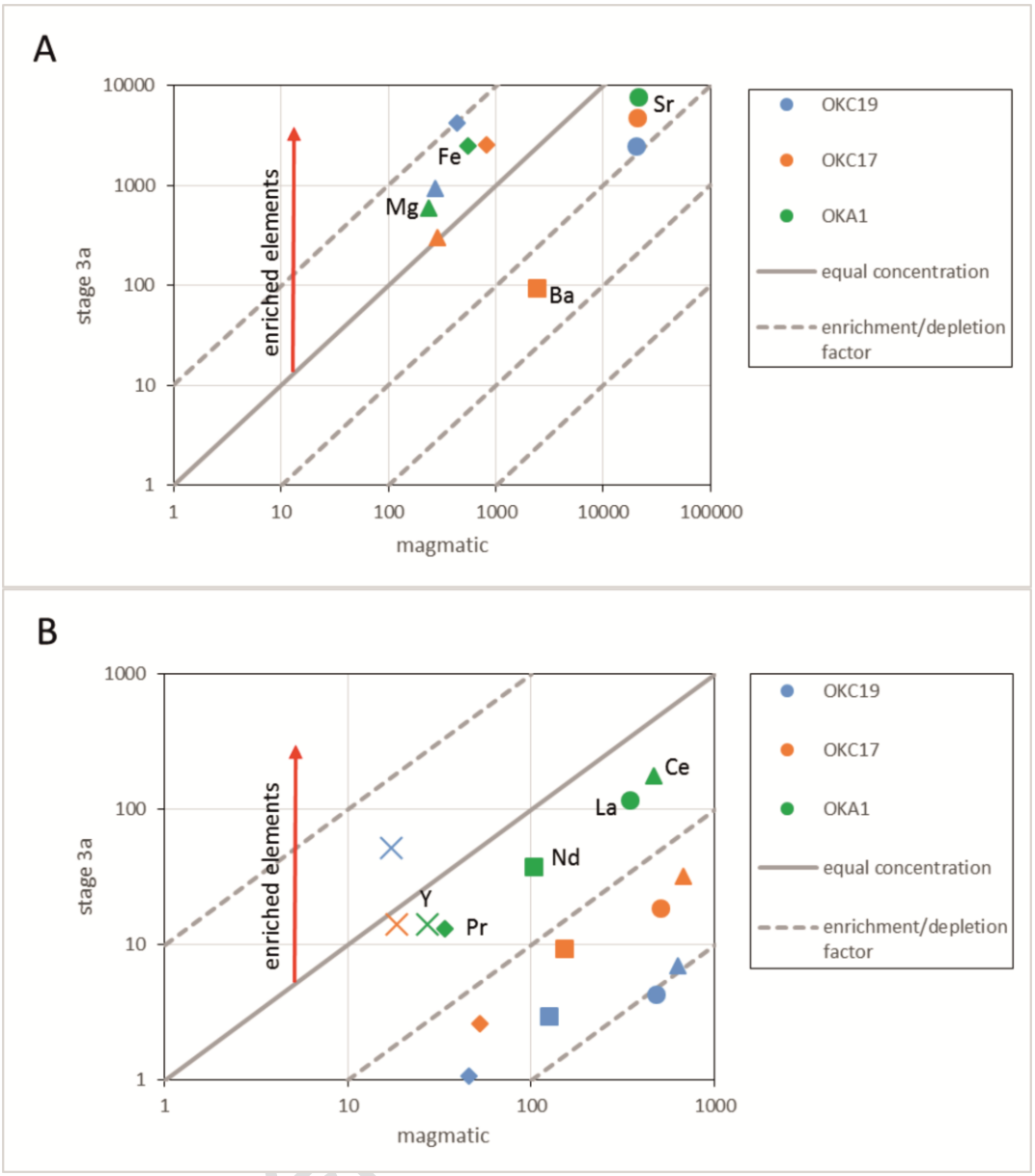

FIG. 9. Comparisons of the composition of magmatic and hydrothermal (stage 3a) calcite to illustrate the changes accompanying recrystallisation. Compositions plotted are element ppm. The calcite carbonatite samples are described in Table 1. (A) Major elements including Sr and Ba (Table 2); (B) Binary plot of the average trace element of the magmatic and stage 3a calcite of the diopside-bearing and pegmatitic calcite carbonatites. Data are in ppm from EPMA and LA-ICP-MS analyses. The different samples are colour coded, and each shape represent one element.

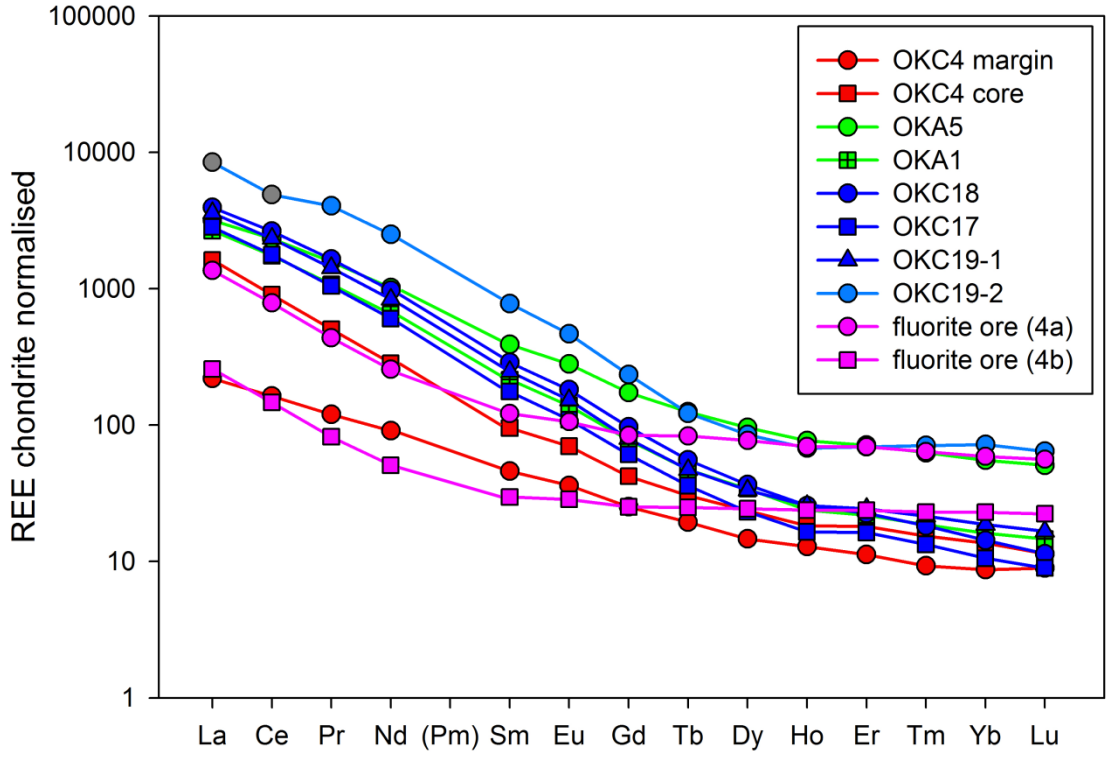

FIG. 10. Whole rock data showing REE chondrite normalised pattern of the Okorusu igneous rocks and fluorite body (McDonough and Sun, 1995). Note that the true Ce and La value of the intensely altered calcite carbonatite (OKC19-2) are higher than the recorded ones (grey) due to the instrument saturation (respectively 2000 ppm and 3000 ppm) and the symbol colours are independent from Fig. 7.

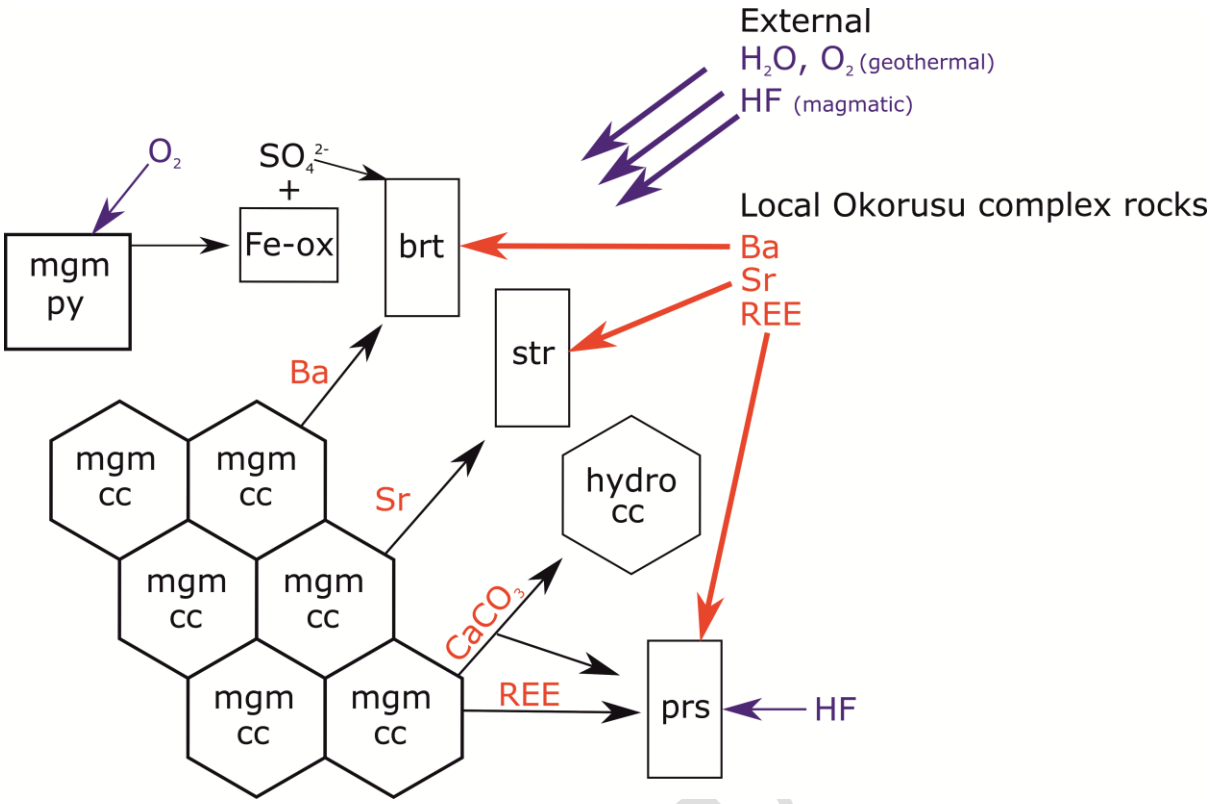

FIG. 11. Schematic presentation of the formation of the main hydrothermal assemblage observed in the altered Okorusu calcite carbonatites. Abbreviations: Fe-ox–unidentified Fe-hydroxide; cc–calcite; mgm–magmatic; hydro—hydrothermal; str—strontianite; prs—parisite; py—pyrite; brt—baryte.

TABLE 1. Summary of the mineralogy of the samples studied (see Figs 2 and 3 for locations). The minerals are listed by order of abundance (only the most abundant hydrothermal minerals are listed here). Note that the estimate percentage of the igneous minerals refers to the entire calcite carbonatite rock including the hydrothermal minerals.

Sample number	Coordinate	Rock type	Igneous mineralogy	Hydrothermal mineralogy
OKC4	20°2'33"S 16°44'22"E	Mafic dyke with chilled margin	Ca-Mg bearing aluminium silicate (5%),diopside (5%), magnesiochromite (<5%), fosterite (<5%)	Actinolite, phlogopite, sodalite, magnetite, pyrite. Total = 80%
OKC4'	20°2'33"S 16°44'22"E	Calcite carbonatite replacing the mafic dyke	Calcite (60%), apatite (<5%)	Calcite, witherite, strontianite, REE-carbonate. Total = 35%
OKA5	20°2'57"S 16°44'39"E	Diopside-bearing calcite carbonatite pod	Calcite (40%), diopside (30%), apatite (15%), phlogopite (5%), pyrite (5%)	Calcite, iron oxide. Total = 5%
OKA1	20°2'57"S 16°44'39"E	Diopside-bearing calcite carbonatite pod	Calcite (25%), diopside (20%), apatite (15%), Ti-bearing magnetite (5%)	Calcite, dolomite, quartz, iron hydroxide, K-feldspar, strontianite, baryte, parisite, witherite, pyrite, REE-carbonate, REE-fluorcarbonate. Total = 35%
OKC17, OKC18, OKC19-1	20°2'34"S 16°44'26"E	Pegmatitic calcite carbonatite pod	Calcite (45%), apatite (<10%), Ti-bearing magnetite (<5%), Nb-bearing mineral (<5%)	Calcite, iron hydroxide, dolomite, pyrite, quartz, K-feldspar, celestine, baryte, strontianite, parisite, REE-carbonate, fluorite. Total = 45% – 65%
OKC19-2	20°2'34"S 16°44'26"E	Intensely hydrothermally altered calcite carbonatite margin	Apatite (<5%)	Calcite (50%), quartz, dolomite, iron hydroxide, baryte, strontianite, celestine-baryte, parisite. Total > 95%
OKC3, OKC6, OKC7, OKC8, OKC10	20°2'31"S 16°44'24"E	Fluorite-rich rock	empty cell	Fluorite (>60 %), calcite, quartz, K-feldspar, dolomite, baryte, parisite. Total = 100%

TABLE 2. Average LA-ICP-MS analyses of magmatic and stage 3a hydrothermal calcite from the Okorusu calcite carbonatites. Note: the LA-ICP-MS data were calculated using the calcium content determined by EPMA. n.d. = not detected, analysis below LA-ICP-MS detection limit. U is below detection for all analyses. Abbreviations: m-magmatic; stg 3a-stage 3a; SD-one standard deviation.

empty cell	OKC4		OKA5		OKA1			OKC17			OKC19-1		OKC19-2	
empty cell	**m**		**m**		**m**		**stg 3a**	**m**		**stg 3a**	**m**		**stg 3a**	
empty cell	n = 15		n = 19		n = 20		n= 7	n= 18		n= 10	n = 5		n = 27	
empty cell							**wt%**							
CaO	52.98		52.32		52.34		54.45	53.97		55.77	53.44		54.15	
SrO	1.36		2.05		2.55		0.89	2.49		0.55	2.39		0.29	
BaO	0.43		0.34		0.23		n.d.	0.27		0.01	0.23		n.d.	
MnO	0.19		0.05		0.07		0.16	0.09		0.16	0.05		0.59	
FeO	0.24		0.01		0.07		0.31	0.11		0.32	0.06		0.53	
MgO	0.22		0.01		0.04		0.10	0.05		0.05	0.05		0.15	
empty cell							**pfu**							
Ca	0.97		0.98		0.97		0.98	0.97		0.99	0.97		0.98	
Sr	0.01		0.02		0.02		0.01	0.02		0.005	0.02		0.003	
Ba	0.003		0.002		0.002		n.d.	0.002		<0.001	0.002		n.d.	
Mn	0.003		<0.001		0.001		0.00	0.001		0.002	0.001		0.01	
Fe	0.003		<0.001		0.001		0.00	0.001		0.004	0.001		0.01	
Mg	0.01		<0.001		0.001		0.00	0.001		0.001	0.001		0.004	
empty cell	avg	SD	avg	SD	avg	SD	avg	SD	avg	SD	avg	SD	avg	SD
empty cell							**ppm**							
Na	152	122	n.d.	n.d.	n.d.	empty	123	86	146	60	n.d.	n.d.	146	16	n.d.	n.d.

This is a 'preproof' accepted article for Mineralogical Magazine. This version may be subject to change during the production process.
DOI: 10.1180/mgm.2019.54

						cell										
La	482	372	314	55	344	138	117	27	508	121	19	12	482	32	4	3
Ce	570	450	414	86	468	175	175	44	679	143	32	20	630	37	7	6
Pr	41	33	32	9	34	13	13	3	53	12	3	2	46	3	1	2
Nd	111	89	95	30	103	38	37	7	151	31	9	6	126	8	3	6
Sm	13	11	9	5	10	3	n.d.	empty cell	12	3	n.d.	empty cell	11	2	<1	<1
Eu	4	3	2	1	3	1	n.d.	empty cell	3	1	n.d.	empty cell	3	<1	<1	<1
Gd	10	8	5	5	9	4	3	<1	8	2	n.d.	empty cell	8	1	1	1
Tb	1	1	n.d.	empty cell	1	<1	n.d.	empty cell	1	<1	n.d.	empty cell	1	<1	<1	<1
Dy	7	5	n.d.	empty cell	5	1	2	<1	3	1	1	1	2	<1	4	1
Ho	1	1	n.d.	empty cell	1	<1	n.d.	empty cell	<1	<1	<1	<1	1	<1	1	<1
Er	5	3	n.d.	empty cell	2	1	n.d.	empty cell	1	1	1	1	1	1	7	3
Tm	1	1	n.d.	empty cell	n.d.	empty cell	n.d.	empty cell	n.d.	empty cell	n.d.	empty cell	n.d.	empty cell	6	5
Yb	6	4	n.d.	empty cell	n.d.	empty cell	n.d.	empty cell	n.d.	empty cell	2	1	1	<1	19	11
Lu	n.d.	empty cell	n.d.	empty cell	n.d.	empty cell	n.d.	empty cell	n.d.	empty cell	n.d.	empty cell	n.d.	empty cell	3	2
Y	57	18	15	7	27	5	14	7	19	2	14	12	17	1	51	26
Th	n.d.	empty cell	n.d.	empty cell	n.d.	empty cell	n.d.	empty cell	n.d.	empty cell	n.d.	empty cell	n.d.	empty cell	n.d.	empty cell

TABLE 3. Average apatite analyses for the Okorusu igneous rocks. Note: CaO, and P_2O_5 and Cl were determined by EPMA and Ca was used to calculate the LA-ICP-MS analyses. n.d. = not detected, analysis below LA-ICP-MS detection limit; SD-one standard deviation.

empty cell	OKC4		OKA5		OKA1		OKC17		OKC19-1		OKC19-2	
empty cell	n = 4		n = 31		n = 29		n= 52		n= 9		n= 31	
empty cell						**wt%**						
CaO	53.20		53.75		54.30		53.75		53.13		52.98	
SrO	1.84		1.56		1.48		1.89		1.73		2.01	
Na2O	0.57		0.06		0.06		0.1		0.14		0.11	
MgO	0.17		0.01		<0.01		<0.01		0.01		0.01	
SiO2	n.d.		n.d.		n.d.		n.d.		0.26		0.36	
P2O5	40.65		39.93		40.06		40.04		40.43		39.95	
Cl	0.03		0.01		0.01		< 0.01		0.01		< 0.01	
empty cell						**cation per 25 O (pfu)**						
Ca	9.84		10		10.03		9.97		9.87		9.90	
Sr	0.15		0.14		0.16		0.16		0.17		0.20	
Na	0.13		0.02		0.02		0.03		0.05		0.04	
Si	n.d.		n.d.		n.d.		n.d.		0.06		0.05	
P	5.94		5.84		5.84		5.87		5.90		5.93	
empty cell	avg	SD	avg	SD	avg	SD	avg	SD	avg	SD	avg	SD
empty cell						**ppm**						
Mn	183	35	122	34	105	36	130	33	n.a.	empty cell	n.a.	empty cell
Fe	419	57	89	41	47	17	69	30	n.a.	empty cell	n.a.	empty cell
K	n.d.	n.d.	n.d.	n.d.	n.d.	n.d.	n.d.	n.d.	n.a.	empty cell	n.a.	empty cell
Ba	143	59	69	11	74	20	97	30	70	9	85	60
La	7069	118	4469	1129	4069	1282	4301	870	3522	1173	4223	1973

Ce	11473	1599	7778	2302	7123	2419	8291	1676	8955	3834	9987	4328
Pr	960	143	691	196	574	214	789	172	763	185	773	256
Nd	2962	426	2260	640	1838	698	2546	579	2425	479	2449	743
Sm	358	54	238	65	197	77	238	55	259	28	264	69
Eu	89	19	56	17	47	20	55	13	61	6	63	18
Gd	260	41	159	39	137	59	148	37	217	32	221	69
Tb	28	4	16	5	13	6	13	3	17	3	18	9
Dy	127	29	72	26	58	26	51	10	66	14	83	56
Ho	21	5	12	5	9	4	8	2	10	2	14	11
Er	45	16	30	13	23	9	16	5	22	7	34	31
Tm	5	1	3	1	2	1	2	1	3	1	4	4
Yb	15	2	17	10	14	6	9	4	10	3	17	17
Lu	n.d.	empty cell	2	1	2	1	1	<1	1	0	2	2
Y	447	7	282	116	221	100	201	46	290	78	419	380
Th	697	123	3097	1558	1584	817	1322	423	815	305	995	676
U	n.d.	empty cell	18	18	15	7	12	10	2	< 2	9	13

TABLE 4. Bulk rock analyses of the Okorusu igneous rocks described in Table 1, OKC4 is a mafic dyke with OKC4m = OKC4 dyke margin and OKC4c = OKC4 dyke core. LREE= La to Sm, HREE= Eu to Lu + Y. Ge, Sn, In, Ag, Ti, Cs and Bi are under 2 ppm; Sb, Be, Hg, Ta and U are under 10 ppm and Ga, As, W, Sc, Rb, Mo and Co are under 60 ppm. BaO and SrO were calculated from the trace element values.

empty cell	OKC4m	OKC4c	OKA5	OKA1	OKC18	OKC17	OKC19-1	OKC19-2
empty cell				**Major elements (wt%)**				
F	0.11	0.58	0.49	0.46	0.42	0.37	0.31	0.13
SiO_2	41.38	27.49	35.94	24.07	3.62	0.79	1.00	19.03
Al_2O_3	10.44	6.91	4.14	0.49	0.18	0.03	0.07	0.06
Fe_2O_3(T)	8.72	7.29	9.10	19.65	2.28	1.75	1.41	1.42
MnO	0.16	0.22	0.47	0.67	0.13	0.11	0.15	0.51
MgO	13.25	9.71	6.55	5.44	0.83	0.22	0.34	0.21
CaO	14.45	21.28	26.24	27.99	49.29	51.93	51.29	36.58
BaO	0.13	0.72	0.09	0.13	0.26	0.29	0.35	4.55
SrO	0.14	0.69	0.49	0.86	> 1.18	> 1.18	> 1.18	> 1.18
Na_2O	3.55	4.75	2.21	0.55	0.10	0.04	0.01	< 0.01
K_2O	1.76	1.60	0.80	0.28	0.10	0.02	0.01	0.03
TiO_2	1.06	0.75	0.85	1.34	0.08	0.07	0.03	0.01
P_2O_5	0.42	0.91	6.75	4.56	4.95	2.82	2.85	0.11
LOI	4.82	17.39	6.79	13.69	34.91	38.41	38.77	30.55
BaO/CaO	0.009	0.034	0.003	0.005	0.005	0.006	0.007	0.124
SrO/CaO	0.01	0.03	0.02	0.03	empty cell	empty cell	empty cell	empty cell
Total - (BaO+SrO)	**100.12**	**98.88**	**100.33**	**99.19**	**96.89**	**96.56**	**96.24**	**88.64**
empty cell				**Trace elements (ppm)**				
V	207	149	244	517	50	50	36	36
Ba	1183	6442	783	1119	2349	2605	3093	40720

Sr	1180	5804	4266	7242	> 10000	> 10000	> 10000	> 10000
Zr	118	68	84	92	28	4	10	< 2
Cr	780	510	30	< 20	< 20	< 20	< 21	< 20
Ni	310	220	30	< 20	< 20	< 20	< 21	< 20
Cu	100	50	50	20	10	20	30	< 10
Zn	60	90	145	340	< 30	30	< 31	< 30
Nb	51	67	199	43	38	30	35	13
Pb	6	26	13	47	12	15	12	138
Th	20	42	180	64	130	50	112	270
La	52	386	759	632	933	671	861	> 2000
Ce	100	554	1445	1070	1620	1090	1440	> 3000
Pr	11	47	148	100	153	97	133	375
Nd	42	130	467	297	445	276	382	1140
Sm	7	14	58	32	43	26	37	115
Eu	2	4	16	8	10	6	9	26
Gd	5	8	34	15	19	12	16	47
Tb	1	1	4	2	2	1	2	4
Dy	4	6	24	8	9	6	8	21
Ho	1	1	4	1	1	1	1	4
Er	2	3	12	4	4	3	4	11
Tm	<1	<1	2	<1	<1	<1	1	2
Yb	1	2	9	3	2	2	3	12
Lu	<1	<1	1	<1	<1	<1	<1	2
Y	20	33	113	40	43	30	46	130
∑LREE	211	1131	2877	2131	3194	2160	2852	> 6630
∑HREE	15	25	106	41	48	30	43	128